Doctoral Thesis

Rheology of short chain branched ring and entangled linear polymers using Molecular Dynamics and Monte Carlo simulation

Eun Jung Roh

Department of Chemical Engineering

Graduate School of UNIST

2020

Rheology of short chain branched ring and

entangled linear polymers using

Molecular Dynamics and

Monte Carlo simulation

Eun Jung Roh

Department of Chemical Engineering

Graduate School of UNIST

Rheology of short chain branched ring and entangled linear polymers using Molecular Dynamics and Monte Carlo simulation

A thesis/dissertation
submitted to the Graduate School of UNIST
in partial fulfillment of the
requirements for the degree of
Doctor of Philosophy

Eun Jung Roh

06. 16. 2020 of submission

Approved by

—————————————————

Advisor

Chunggi Baig

Rheology of short chain branched ring and entangled linear polymers using Molecular Dynamics and Monte Carlo simulation
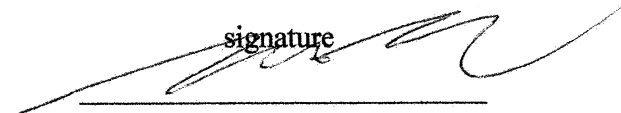
Eun Jung Roh

This certifies that the thesis/dissertation of Eun Jung Roh is approved.
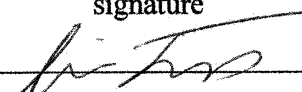
06. 16. 2020

signature

Advisor: Chunggi Baig

signature

So Youn Kim

signature

Jaeup Kim

signature

Jiseok Lee

signature

Hankown Lim

Abstract

  In view of the fact that human history can be divided into eras according to the primary materials such as stone age, bronze age, and iron age, we can definitely say that we are living in the polymer age. The advanced polymeric materials are widely used in different fields of science, technologies and industries. For instance, there are biopolymers and therapeutic polymers, synthetic fibers, 3D printing plastics, polymeric films and membranes. As their applications are highlighted, study on characterizing the structural and rheological properties of polymers becomes one of the most important issue, because such knowledge enables to tailor material properties and control physical phenomena as required. However, due to their enormous intramolecular degree of freedom, polymers generally exhibit a variety of complex structural and rheological behaviors such as shear thinning and thickening, strain hardening, melt fracture, and phase separation. To understand the physical properties for polymer solutions and melts, we need to look into how polymeric materials behave on microscopic level, investigate molecular mechanisms behind those complex phenomena, and properly analyze what determines macroscopic properties. In this regard, computational study is essential for understanding the complicated macroscopic behaviors at the fundamental level. Depending on the time and length scales of polymer systems, there are multiple simulation methods. In this thesis, the molecular dynamics (MD) simulations based on the Newton's second law and Monte Carlo (MC) simulations exploiting statistical mechanics are hired to carry out the detailed analysis on the physical properties of polymeric melts at atomistic level.

  This research is subdivided into three specific subjects. First, the structural and rheological properties of ring polymers at dense melt and dilute solution systems are analyzed under the steady shear flow using atomistic molecular dynamics simulations. Second, the effects of short-chain branching (SCB) on the unentangled ring and linear polyethylene are investigated at equilibrium state. Third, the new nonequilibrium Monte Carlo simulation methodology has been developed based on expanded nonequilibrium thermodynamic formalism to enhance to overcome the time-consuming problem of classical MD simulations.

Contents

List of Figures

[CH_2-CH-CH_2-CH_2 (SET 1, black), CH-CH_2-CH_2-CH_2 (SET 2, yellow), and CH_2-CH_2-CH_2-CH_2 (SET 3, green)] are separately plotted. The bare linear and ring PE systems are represented by 'Linear' and 'Ring', respectively.

Figure 2.3.4. Mean squared amplitude of the Rouse normal modes $<X_p{}^2>$ as a function of N/p^2 (N being the number of backbone atoms) for (a) the bare and SCB linear PE, and (b) the bare and SCB ring PE melt systems. The blue dash line of slope 1 corresponds to the ideal Rouse behavior based on eqn (2.3.3).

Figure 2.3.5. Normalized time autocorrelation functions of the first seven normal modes as a function of p^2t: (a) p = 1, 2, 3, 4, 5, 6, and 7 for the bare and SCB linear systems, and (b) p = 2, 4, 6, 8, 10, 12, and 14 for the bare and SCB ring systems. The orange symbols represent the ideal Rouse behavior based on eqns (2.3.4) and (2.3.5).

Figure 3.3.1. Schematic description of the numerical algorithm for constructing intrinsic ring surface.

Figure 3.3.2. Rotational illustrations of the toy model under shear flow without the Brownian random force. (A) When there is no surface area facing the yz-plane at the initial state. (B) When there is non-zero surface area facing the yz-plane at the initial state. The yellow arrows in the illustrations indicate the normal vector of the toy model.

Figure 3.3.3. (Left) Area projected from the intrinsic surface of the ring into three xy- (circles and dashed line), xz- (squares and solid line), and yz- (triangles and dotted line) planes for melt (orange symbols), dilute (black symbols), and toy model (dark green lines) as a function of Weissenberg number (Wi). Note that these projected areas were normalized by the total area of the intrinsic ring surface A_t. (Right) The ratio between A_{xy} and A_{xz} vs. Wi for melt (orange circles), dilute (black circles), and toy model (dark green line).

Figure 3.3.4. Molecular mechanisms of ring polymer. (A) Schematic illustrations for the fundamental molecular dynamics mechanisms for the ring polymer under shear flow. (B) Representative results of the average accumulated angle θ_n of $\mathbf{n}_{avg}$, θ_{xy} of $\mathbf{Q}_{xy}$ projected on the xy-plane, and θ_{yz} of $\mathbf{Q}_{yz}$ projected on the yz-plane during loop migration (left panel), end-loop tumbling (middle panel), and center-loop tumbling (right panel).

Figure 3.3.5. (Left) The proportion of the end-loop tumbling (circles) and center-loop tumbling (triangles) mechanisms as a function of Wi for the dilute (black) and melt (orange) ring systems. (Right) Probability distribution function (PDF) of the chain radius of gyration normalized by the equilibrium value for the ring (black line) and linear (dark green line) PE melts in the strong flow regime at Wi = 100 and 2000, respectively.

Figure 4.3.1. Comparison of the (a) *xx*, (b) *xy*, and (c) *yy* components of the thermodynamic force field α between the entangled $C_{400}H_{802}$ and unentangled ($C_{50}H_{102}$, $C_{78}H_{158}$, $C_{128}H_{258}$) polyethylene melts as a function of De number. The error bars are smaller than the size of the symbols.

Figure 4.3.2. Comparison between GENERIC MC and NEMD for the *xx*, *xy*, *yy*, and *zz* components of the conformation tensor $\tilde{\mathbf{c}}_{ete}$ as a function of De number for the simulated $C_{400}H_{802}$ entangled PE melt. The error bars are smaller than the size of the symbols unless specified otherwise.

Figure. 4.3.3. (a) Comparison of the probability distribution function (PDF) of the chain end-to-end distance $|\mathbf{R}_{ete}|$ between GENERIC MC (dashed lines) and NEMD (solid lines) for the simulated $C_{400}H_{802}$ entangled PE melt at various De numbers. For clarity, the results at high De numbers are presented separately in the inset. To alleviate the influence of polydispersity for the GENERIC MC simulations, only chains whose length is in the range $C_{350}H_{702}$–$C_{450}H_{902}$ were included in the calculation.(b) Comparison between GENERIC MC (dashed lines) and NEMD (solid lines) for the probability distribution of the orientation angle of the chain end-to-end vector (θ_{ete}) with respect to the flow direction as a function of De number.

Figure 4.3.5. Comparison between GENERIC MC (filled symbols) and NEMD (open symbols) for the distribution of the six representative mesoscale chain configurations (Fold, Half-dumbbell, Stretched, Kink, Dumbbell, and Coil) obtained by the Brightness method at various De numbers. A simple conformation sketch for the six mesoscale chain structures is presented above the plot.

Figure 4.3.6. Comparison between GENERIC MC and NEMD for the representative topological measures obtained by the Z1-code at various De numbers; the average primitive path (PP) contour length $\langle L_{pp} \rangle$, the average number of entanglement strands $\langle Z_{es} \rangle$ per chain, the average end-to-end length $\langle d_{es} \rangle$ of an entanglement strand, and the average number of carbon atoms $\langle N_{es} \rangle$ per entanglement strand. The GENERIC MC results involve selective chain lengths in the range of $C_{380}H_{762}$ to $C_{420}H_{842}$ to relieve the influence of polydispersity.

Figure. 4.3.7. Comparison between GENERIC MC and NEMD for (a) the average orientation angle based on entanglement segment vector $\langle \theta_{es} \rangle$ and (b) the average number of entanglement (kink) points $\langle Z_{kink} \rangle$ (normalized by the equilibrium value) with respect to the (normalized) PP contour segment *s* ranging from 0 to 1. For adequate comparison, only the chains whose length is in the range $C_{380}H_{762}$–$C_{420}H_{842}$ were involved in the GENERIC MC results.

List of Tables

Nomenclature

Symbol	Description	Unit
$\dot{\gamma}$	Applied shear rate	1/ns
λ	Longest characteristic relaxation time	ns
Wi	Weissenberg number	
De	Deborah number	
L_x, L_y, L_z	Simulation box length x, y, and z	Å
$\sigma_{LJ}, \varepsilon_{LJ}$	Lennard-Jones interaction parameter of fluid	
H	Hamiltonian	
m, **a**, **v**	Mass, acceleration and velocity	g, m/s^2, m/s
p, **q**, t	Momentum vector, position vector, and time	g m/s, Å, ns
ρ	Density	g/cm^3
$<R_d^2>$, $<R_{ete}^2>$, $<R_g^2>$	Mean square of ring diameter, end-to-end vector, and radius of gyration	Å^2
φ	Bond-torsional angle	degree
p	Rouse normal mode	
$\mathbf{X}_p$	Rouse normal coordinate of normal mode p	Å
τ_p	Characteristic relaxation time of normal mode p	ns
$g(r)$	Pair distribution function	
U, A	Internal potential energy, Helmholtz free energy	J
T, S, P, V	Temperature, Entropy, Pressure, Volume	K, J, Pa, m^3
N_{ch}	Number of polymer chains	
N_{seg}	Number of entanglement segment	
k_B	Boltzmann constant	J/K
$\boldsymbol{\alpha}$	Thermodynamic force field	
$\tilde{\mathbf{c}}_{ete}$	Conformation tensor based on end-to-end vector	
$\tilde{\mathbf{c}}_{seg}$	Conformation tensor based on entanglement segment vector	
σ	Shear stress	MPa
L_{pp}	Primitive path contour length	Å
Z_{es}	Number of entanglement strands per chain	

d_{es}	End-to-end length of an entanglement strand	Å
N_{es}	Number of monomers per entanglement strand	
Z_{kink}	Number of kink points per chain	
θ_{ete}	Orientation angle of end-to-end vector	degree
θ_{es}	Orientation angle of entanglement segment	degree
η	Shear viscosity	Pa s
Ψ_1, Ψ_2	First and second normal stress coefficient	Pa s^2
$\mathbf{n}_{avg}$	Average normal vector	
$A_t, A_{xy}, A_{xz}, A_{yz}$	Total area of ring surface and projected on each plane	Å^2

Chapter 1. Introduction

1.1. Research Motivation

Understanding the structural and dynamical behavior of polymer liquids becomes imperative, since the advanced polymer materials are widely applied for the modern technologies and industries. Furthermore, the development process for the novel polymeric materials breaks from the conventional trial and error relying on the empirical data and goes forward to the inverse design strategy where the material architecture is formulated to intrinsically have the desirable properties.

The enormous efforts have been made to comprehend the general knowledge of the structure-property-phenomenon relationship. The significant advances have been achieved in elucidating the stress relaxation of linear and long-chain branched (LCB) polymers. [1-4] However, there is still critical lack of the understanding on the effects of the closed-loop topology on ring polymers. Despite the ring polymer is essentially characterized as a linear except that two free ends are connected, the structural and dynamical properties are significantly changed. Therefore, the comprehensive analysis with the new viewpoint of that ring polymers intrinsically possess two-dimensional surface characteristics is needed to understand their fundamental structural characteristics and dynamic mechanisms behind distinctive macroscopic properties. In addition, role of short branches whose length is even below Kuhn length has not been well understood, because the standard entropic approach is inapplicable. Recently, the numerical studies find out the essential role of short branches disturbing the overall chain conformation via fast random movement. [5] Under the various types of external flow, short chain branched (SCB) polymers commonly exhibit the compact structure and resistance of structural deformation against the applied flow. [5-8] In order to analyze the effects of short branches on the structural compactness, the additional study at fundamental atomistic level is needed to be carried out.

Meanwhile, in the computational study for polymer systems, the classical MD simulations are limitedly used for the rather short chain polymers compared to those in practical applications, because time tracking of the large systems requires long simulation time unreachable by most advanced computing systems. [9] When the efficient Monte Carlo simulation is established on the nonequilibrium thermodynamics [10-14], this new method can solve the time consuming problem and further contribute to efficient study for the large molecular systems.

1.2. Theoretical Backgrounds

1.2.1. Polymer Physics

As a part of macromolecular science, the polymer physics begins with the study for the effects of long-chain connectivity between monomers. The early experiment and theoretical research have concentrated on the dilute polymer systems at the equilibrium state. Now, the polymer physics goes beyond the dilute systems and extensively deals with the polymers in the solid state and concentrated systems using molecular models and the statistical mechanics methods. It essentially aims to understand the structure-property relationship in order to tailor the material properties such as elasticity, crystallinity, and tensile strength as required and further control the physical phenomena.

There are two well-known models successfully describing the structural and dynamical behaviors for unentangled and entangled polymer melts. For the unentangled polymers, their basic structure and dynamics can be described by the Rouse model which assumes a polymer chain as a set of beads connected by the entropic springs. [2,15,16]
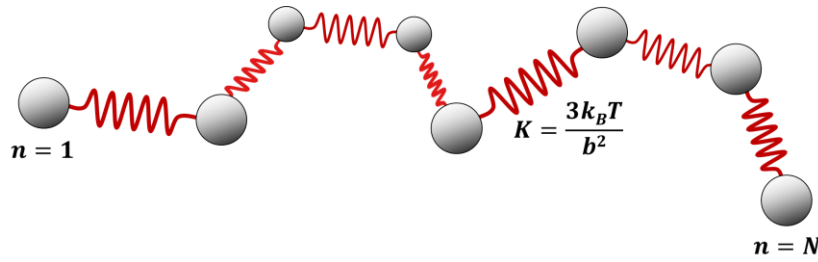
Figure 1.2.1. Schematic description of the Rouse model with N number of beads (gray circles) connected by springs.

In other words, in this model, the dynamics of polymer is governed by the only intermolecular interactions with two neighboring beads. Specifically, the beads are characterized by hydrodynamic friction coefficient ξ and spring constant $\dfrac{3k_BT}{b^2}$ is obtained from the Helmholtz free energy where potential energy is ignored and only entropic effect is concerned. Then, the Langevin equation gives

$$\zeta \frac{\partial \mathbf{R}_n}{\partial t} = \frac{3k_BT}{b^2}\frac{\partial^2 \mathbf{R}_n}{\partial n^2} + \mathbf{f}_n \quad \text{for } n = 1, 2, \ldots, N \tag{1.2.1}$$

where $\mathbf{R}_n$ is the position of bead n, $\mathbf{f}_n$ is random force, k_B is Boltzmann constant, b is average length of spring and N is the number of beads. According to the molecular architecture, the boundary condition is different. For linear polymers,

$$\left.\frac{\partial \mathbf{R}_n}{\partial n}\right|_{n=0} = 0 \quad \text{and} \quad \left.\frac{\partial \mathbf{R}_n}{\partial n}\right|_{n=N} = 0 \tag{1.2.2}$$

To contrary, for ring polymers,

$$\left.\frac{\partial \mathbf{R}_n}{\partial n}\right|_{n=0} = \left.\frac{\partial \mathbf{R}_n}{\partial n}\right|_{n=N} \quad \text{and} \quad \mathbf{R}_0 = \mathbf{R}_N \tag{1.2.3}$$

The Langevin equation can be solved with boundary conditions using Fourier transform of $\mathbf{R}_n(t)$ into the normal coordinate $\mathbf{X}_p(t)$ defined as:

$$\mathbf{X}_p(t) = \frac{1}{N}\int_0^N \mathbf{R}_n(t)\cos\left(\frac{p\pi n}{N}\right)dn \tag{1.2.4}$$

where linear chain has only odd modes of p (i.e., $p = 1, 3, 5, \ldots$) and ring chain has only even modes of p (i.e., $p = 0, 2, 4, \ldots$). Finally, the structural and dynamical properties estimated by Rouse model are summarized in below table.

Table 1.2.1. Structure and dynamical properties (i.e., end-to-end distance $<R_{ete}{}^2>$, ring diameter $<R_d{}^2>$, radius of gyration $<R_g{}^2>$, relaxation time τ_R, and zero-shear viscosity η_0) for linear and ring polymer chains estimated by Rouse model.

	Linear	Ring
$\left\langle R_{ete}{}^2 \right\rangle$	Nb^2	-
$\left\langle R_d{}^2 \right\rangle$	-	$\dfrac{1}{4}Nb^2$
$\left\langle R_g{}^2 \right\rangle$	$\dfrac{1}{6}Nb^2$	$\dfrac{1}{12}Nb^2$
τ_R	$\dfrac{1}{3}\dfrac{\zeta N^2 b^2}{\pi^2 k_B T}$	$\dfrac{1}{12}\dfrac{\zeta N^2 b^2}{\pi^2 k_B T}$
η_0	$\dfrac{\pi^2}{12}\dfrac{\rho RT}{M}\tau_{R,linear}$	$\dfrac{\pi^2}{6}\dfrac{\rho RT}{M}\tau_{R,ring}$

For the entangled polymers, topological constraint imposed by surrounding chains to the target chain plays an important role in polymer dynamics, because it significantly reduces the dynamical degrees of freedom. Therefore, beyond the intrinsic polymer properties characterized by hydrodynamic coefficient ζ and size of the chain Nb, additional topological constraint effect should be taken into account. According to the tube model [1,2], the intermolecular topological interactions are approximated as a mean-field tube whose axis coincide with that of the chain primitive path (i.e., the geometrically constructed shortest path connecting two chain ends without violating topological constraints).
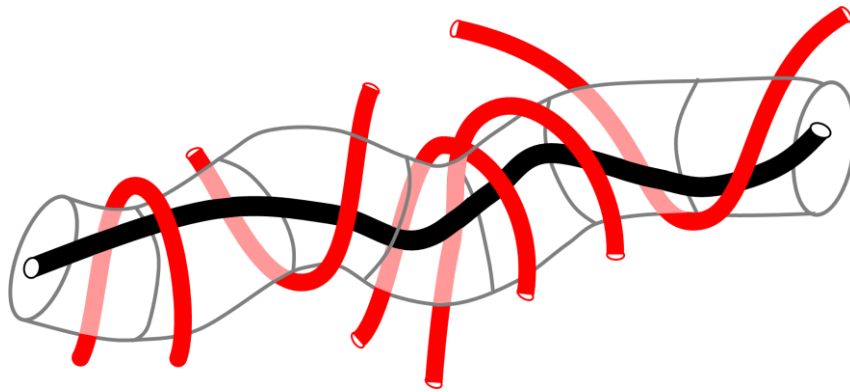
Figure 1.2.2. Schematic view of tube model where the topological constraints imposed by surrounding red chains to the target black chain are approximated as a mean-field tube.

At short time scale, the dynamics of entangled polymer chain is assumed to be wiggling within the one-dimensional curvilinear tube region characterized by tube diameter of a. However, at long time scale, snake-like reptative chain motion originating from the strong thermal motion of chain ends changes the primitive path by creating and destroying the ends of primitive path. [1] Therefore, the overall dynamics of entangled polymer chain is equivalent to the time evolution of the primitive path and the stress relaxation of entangled polymer chains is described by the survival probability $\psi(s,t)$ of chain segment s to remain inside the initial tube at time t.

Besides chain reptation motion, additional relaxation mechanisms for entangled polymers are investigated to complement the discrepancy between tube theory prediction and some important experimental observations such as scaling behavior of zero-shear viscosity with molecular weight (i.e., $\eta_0 \sim M^3$ for original tube model and $\eta_0 \sim M^{3.4}$ for experimental measurements). [2,17] Generally, there are contour length fluctuation (CLF) which accounts for the variation of the primitive path contour length with time and constraint release (CR) which considers the dynamics of constraint itself. [1,2]

1.2.2. Rheology

Rheology is, literally, the physical science that studies the flow and deformation of the materials. In particular, the non-Newtonian fluids exhibit distinctive rheological response at the non-equilibrium state such as shear-thinning, melt fracture, and rod-climbing effect, because the contrasting viscous properties (following Newton's law) and elastic properties (following Hooke's law) appear simultaneously, called "viscoelasticity". [17,18] To accurately characterize the structural deformation and stress relaxation behavior of the polymeric fluids, the two types of flows are typically used: shear and elongation flow. The velocity field for shear and elongational flow is defined respectively as:

$$v_{shear}(t) = \begin{pmatrix} \dot{\gamma}(t)\,y \\ 0 \\ 0 \end{pmatrix} \tag{1.2.5}$$

$$v_{elongation}(t) = \begin{pmatrix} -\dfrac{1}{2}\dot{\varepsilon}(1+b)\,x \\ \dfrac{1}{2}\dot{\varepsilon}(1+b)\,y \\ \dot{\varepsilon}\,z \end{pmatrix} \tag{1.2.6}$$

Shear flow

Elongational flow

Uniaxial Elongation (b=0, $\dot{\varepsilon}$ >0)

Biaxial Elongation (b=0, $\dot{\varepsilon}$ <0)

Planar Elongation (b=-1)
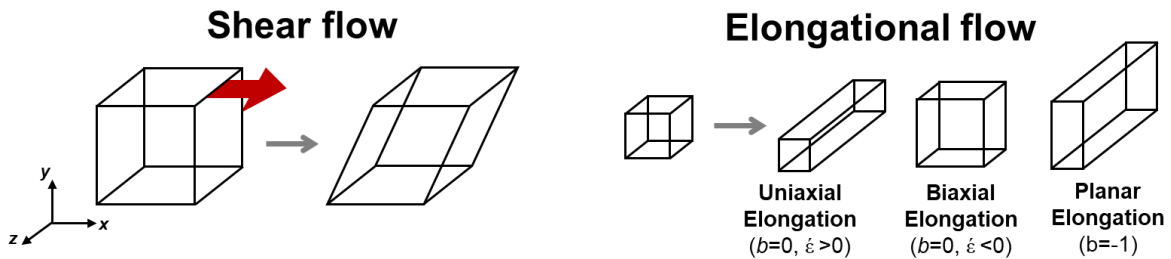
Figure 1.2.3. Schematic illustration for the deformation of a cube in the shear flow (left) and planar elongation flow (right).

The ideal goal of the rheology is to understand the physical material properties at the non-equilibrium state and finally, develop the constitutive equation that can explain and predict the linear and nonlinear viscoelastic behavior of polymer mateirals. The classical approach for developing constitutive equation is generalized linear viscoelastic (GLVE) fluid model formatted as:

$$\tau(t) = -\int_{-\infty}^{t} G(t-t')\dot{\gamma}(t')dt'$$

$$= \int_{-\infty}^{t} M(t-t')\gamma(t,t')dt'$$

(1.2.7)

Here, the nature of the applied external flow is represented by the infinitesimal strain tensor γ and the nature of the material is represented by the relaxation modulus G and memory function M implying that the non-Newtonian fluids remember the past deformation they have experienced and the magnitude of memory effect decreases as one goes in backwards in time. (i.e., fading memory effect). For instance, in case of the Maxwell model which describes the viscoelastic behavior of the fluids by simple combination of dashpot (viscous property) and spring (elastic property), the relaxation modulus is $G(t-t') = \frac{\eta_0}{\lambda}e^{-\frac{1}{\lambda}(t-t')}$ indicating that the material forgets the history exponentially. [17,18] The GLVE approach is valuable in aspects that it is the first attempt for developing constitutive equations with consideration of the memory effect and in addition, can capture the rheological response of the fluids undergoing start-up, cessation, and small amplitude of oscillatory shear (SAOS) limitedly at small strains and weak flow rates. However, it fails to predict the nonlinear response of the material in large-deformation and breaks frame-invariant objectivity.

In order to accurately capture the frame-invariant objectivity, trial for other strain measurement such as Cauchy strain tensor (**c**) and Finger strain tensor (**c**$^{-1}$) is made and that is equivalent to use different time derivatives for stress tensor (i.e., upper-convected time derivative $\overset{\Delta}{\tau}$ or lower-convected time derivative $\overset{\nabla}{\tau}$) in the differential form of the equation. In addition, to account for the nonlinear viscoelasticity, the framework of the constitutive equation is changed from the GLVE by introducing the new terms such as the second order of stress and potential derivatives into the formulation.

Despite this simple empirical modification can match the wider variety of rheological behavior under the flow, the phenomenological development is unmanageable work. Hence, it is necessary to pursue molecular approaches which find some molecular level clues that are useful in interpreting complex phenomena and build up the constitutive equations for the macroscopic stress with reference to the detailed molecular physics.

1.3. Computational study

The computational approach to the soft matter systems can be subdivided into the several hierarchies depending on the different levels of resolution. The simulation methods at each level can cover the specific window of length and time and thus, it is important to choose the simulation methods appropriate for the system of interest. Furthermore, by systematically integrating the methods at different levels, multiscale modeling is beneficial for comprehensive understanding of complex macromolecule properties involving multiplicity of time and length scales.

At the most fundamental level, the quantum simulations such as ab-initio methods and density functional theory (DFT) investigate the electronic structure by solving the Scrhödinger equation ($H\Psi=E\Psi$). Using the invaluable information obtained from quantum simulations such as bonded geometry and electronic properties as input, the atomistic level simulations can estimate the macroscopic structural and dynamical properties and further provide insight the detailed molecular mechanisms behind complex equilibrium and nonequilibrium behavior. [9] The mesoscale simulations employing the coarse-grained representations can deal with longer time and length scale of the system and finally, at the continuum level, the polymer liquids are considered no longer as a collection of polymeric chains but as an entire material.

In this research, the simulations at fundamental atomistic level such as molecular dynamics and Monte Carlo simulation are adopted to analyze and understand the molecular mechanism behind the complicated polymeric phenomena. [19-21]
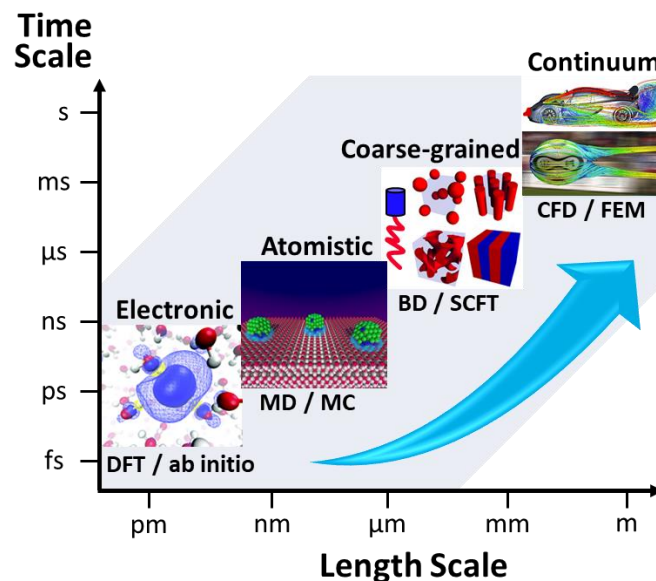
Figure 1.3.1. Hierarchy of multiscale modeling.

1.3.1. Molecular Dynamics simulations

As a one of the most powerful computational methods, molecular dynamics simulation is widely applied to polymeric systems and has proven very beneficial for understanding the complicated macroscopic rheological behaviors of polymer systems at the fundamental molecular level. [11] Molecular dynamics simulation solves classical Newton's laws of motion:

$$\mathbf{F} = m\mathbf{a} = m\frac{d\mathbf{v}}{dt} \tag{1.3.1}$$

where $\mathbf{F}$ is force, $\mathbf{a}$ acceleration, m mass, v velocity of an atom and t is time. And then, tracks position and velocity of individual particles in time and finally provides time averaged thermodynamic properties, structural properties, and rheological properties. The Hamiltonian H of a system can be separated into kinetic energy K and potential energy U as a function of the set of momentum $\mathbf{p}_i$ and coordinates $\mathbf{r}_i$ of each particle i, respectively as follows:

$$H(\mathbf{r},\mathbf{p}) = K(\mathbf{p}) + U(\mathbf{r}) = \sum_{i=1}^{N}\frac{\mathbf{p}_i^2}{2m_i} + U(\mathbf{r}_1,...,\mathbf{r}_N) \tag{1.3.2}$$

Then, the Hamiltonian's equations of motion which governs entire time-evolution of the system can be expressed as:

$$\dot{\mathbf{r}}_i = \frac{\partial H}{\partial \mathbf{p}_i}$$
$$\dot{\mathbf{p}}_i = -\frac{\partial H}{\partial \mathbf{r}_i} \tag{1.3.3}$$

The set of p-SLLOD equations [22] of motion implemented with the Nosé-Hoover thermostat and barostat [23,24] for isothermal-isobaric (NPT) NEMD simulations is as follows:

$$\dot{\mathbf{r}}_i = \frac{\mathbf{p}_i}{m_i} + \mathbf{q}_i \cdot \nabla\mathbf{u}$$

$$\mathbf{p}_i = \mathbf{F}_i - \mathbf{p}_i \cdot \nabla\mathbf{u} - m_i\mathbf{q}_i \cdot \nabla\mathbf{u} \cdot \nabla\mathbf{u} - (\dot{\chi} + \dot{\varsigma})\mathbf{p}_i$$

$$\dot{\chi} = \frac{P_\chi}{Q_\chi}, \quad \dot{P}_\chi = \sum_i^N \mathbf{r}_i \cdot \mathbf{F}_i + \sum_i^N \frac{p_i^2}{m_i} - DNVP, \quad Q_\chi = DNk_BT\tau_b^2 \tag{1.3.4}$$

$$\dot{\varsigma} = \frac{P_\varsigma}{Q_\varsigma}, \dot{P}_\varsigma = \sum_i^N \frac{p_i^2}{m_i} - DNk_BT, Q_\varsigma = DNk_BT\tau_t^2$$

where $\mathbf{r}_i$, $\mathbf{p}_i$, and $\mathbf{F}_i$ are, respectively, the position, momentum, and force vector of the ith atom of mass m_i. ς and P_ς are the coordinate-like and momentum-like variables, respectively, of the Nosé-Hoover thermostat with the thermostat mass parameter Q_ς. Similarly, P_χ, and Q_χ are the co

22

ordinate-like and momentum-like variables, respectively, of the Nose-Hoover barostat with the barostat

mass parameter Q_χ. The relaxation time parameters for the thermostat and barostat were set equal to

τ_b = 1.07 ps and τ_t = 0.24 ps, respectively, for all simulations. D denotes the dimensionality of the

system and k_B Boltzmann's constant. N, V, and P represent the total number of atoms, the volume of

the system, and the total pressure of the system, respectively. And $\nabla \mathbf{u}$ is the following velocity

gradient tensor. For steady shear flow, it has form of:

$$\nabla \mathbf{u} = \begin{pmatrix} 0 & 0 & 0 \\ \dot{\gamma} & 0 & 0 \\ 0 & 0 & 0 \end{pmatrix} \tag{1.3.5}$$

This equations of motions are integrated by an efficient reversible reference system propagation

algorithm (r-RESPA) [25]. The time propagator $\mathbf{G}(\Delta t)$ for atom i can be derived as follows:

$$
\begin{aligned}
\mathbf{G}(\Delta t) = & \exp\left[\frac{\Delta t}{2} F_s \frac{\partial}{\partial p_s}\right] \exp\left[\frac{\Delta t}{4} \mathbf{f}(\mathbf{r}_i) F_s \frac{\partial}{\partial \mathbf{p}_i}\right] \exp\left[-\frac{\Delta t}{2} \frac{p_s}{Q} \mathbf{p}_i \frac{\partial}{\partial \mathbf{p}_i}\right] \\
& \exp\left[\frac{\Delta t}{4} \mathbf{f}(\mathbf{r}_i) F_s \frac{\partial}{\partial \mathbf{p}_i}\right] \exp\left[-\frac{\Delta t}{2} m_i \mathbf{r}_i \cdot (\nabla \mathbf{u}) \cdot (\nabla \mathbf{u}) \frac{\partial}{\partial \mathbf{p}_i}\right] \\
& \exp\left[-\frac{\Delta t}{2} \mathbf{p}_i \cdot (\nabla \mathbf{u}) \frac{\partial}{\partial \mathbf{p}_i}\right] \exp\left[\frac{\Delta t}{2} \frac{s p_s}{Q} \frac{\partial}{\partial s}\right] \exp\left[\frac{\Delta t}{2} \mathbf{r}_i \cdot (\nabla \mathbf{u}) \frac{\partial}{\partial \mathbf{r}_i}\right] \\
& \exp[i\mathbf{L}\Delta t] \exp\left[\frac{\Delta t}{2} \mathbf{r}_i \cdot (\nabla \mathbf{u}) \frac{\partial}{\partial \mathbf{r}_i}\right] \exp\left[\frac{\Delta t}{2} \frac{s p_s}{Q} \frac{\partial}{\partial s}\right] \\
& \exp\left[-\frac{\Delta t}{2} \mathbf{p}_i \cdot (\nabla \mathbf{u}) \frac{\partial}{\partial \mathbf{p}_i}\right] \exp\left[-\frac{\Delta t}{2} m_i \mathbf{r}_i \cdot (\nabla \mathbf{u}) \cdot (\nabla \mathbf{u}) \frac{\partial}{\partial \mathbf{p}_i}\right] \\
& \exp\left[\frac{\Delta t}{4} \mathbf{f}(\mathbf{r}_i) F_s \frac{\partial}{\partial \mathbf{p}_i}\right] \exp\left[-\frac{\Delta t}{2} \frac{p_s}{Q} \mathbf{p}_i \frac{\partial}{\partial \mathbf{p}_i}\right] \\
& \exp\left[\frac{\Delta t}{4} \mathbf{f}(\mathbf{r}_i) F_s \frac{\partial}{\partial \mathbf{p}_i}\right] \exp\left[\frac{\Delta t}{2} F_s \frac{\partial}{\partial p_s}\right]
\end{aligned} \tag{1.3.6}
$$

where Liouville operator $\mathbf{L}$ is defined as follows:

$$i\mathbf{L} = i\mathbf{L}_r + i\mathbf{L}_p = \frac{\mathbf{p}_i}{m_i} \frac{\partial}{\partial \mathbf{r}_i} + \mathbf{F}_i \frac{\partial}{\partial \mathbf{p}_i} \tag{1.3.7}$$

Because $\mathbf{L}_r$ and $\mathbf{L}_p$ are not communicating operators, we cannot simply rewrite $\exp[i\mathbf{L}_r]\exp[i\mathbf{L}_p]$ as

$\exp[i\mathbf{L}_p]\exp[i\mathbf{L}_r]$, but in numerical calculation discretization is inevitable. By choosing Δt smaller,

we can gain more accuracy and consider overall effects of operation on position and momentum.

Furthermore, to make the RESPA reversible in time, the time propagator has to be a symmetric form.

1.3.2. Monte Carlo Simulations

The Monte Carlo (MC) simulation is a stochastic method to solve problems numerically using repeated random samplings. Due to the stochastic characteristics, it is named after the city of Monaco which is famous for its casino and gambling. This method is first developed during the World War II to study the diffusion and collision behavior of neutrons in fission materials. Today, it is widely applied to the fields such as artificial intelligence (AI), financial engineering, bioinformatics, physics and various engineering fields. In particular, the MC is powerful to effectively study the dense phase of polymers at fundamental atomistic level, because the avoidance of tracking the time evolution of actual dynamics of polymer systems enables to jump the huge free-energy barrier separating two regions of configuration space between transient and steady state. [26-33]

The application of MC simulations for polymer systems follows three steps. First, generate an initial configuration and second try a randomly generated configuration relying on random number and unphysical MC movements. At step three, evaluate the new configuration according to the acceptance criteria and random number and then decide whether the new configuration should be accepted or rejected. For the second step, because it is impossible to look into the whole possible configuration space, sampling the preferable state which makes most significant contributions to the system (i.e., importance sampling) is important. This is acquired by development and implementation of efficient MC movements for the polymer configurations. The widely used MC algorithms include reptation, flip, end-mer rotation, concerted rotation, and end-bridging.[34-36] The reptation movement is a traditional and simple move where one end of a randomly selected polymer chain is detached and reattached to the opposite end where the local geometry such as bond length, bending angle, and torsional angle is fixed. The flip and end-mer rotation movement rearrange the torsional angle of internal atoms or bending angle of an end atom of a randomly selected chain, respectively. The concerted rotation movement corresponds intramolecular rebridging movement where the coordinates of bridging trimer and neighboring atoms are switched by adjusting the torsional and bending angles. The advanced end-bridging movement is designed to cut the connectivity of randomly selected two polymeric chains into each two subchains and then exchange the subchains to produce a new chain configuration with constraints of bond length and angle.

Flip Movement

End Bridging Movement

2

1

Before

2'

1'

After
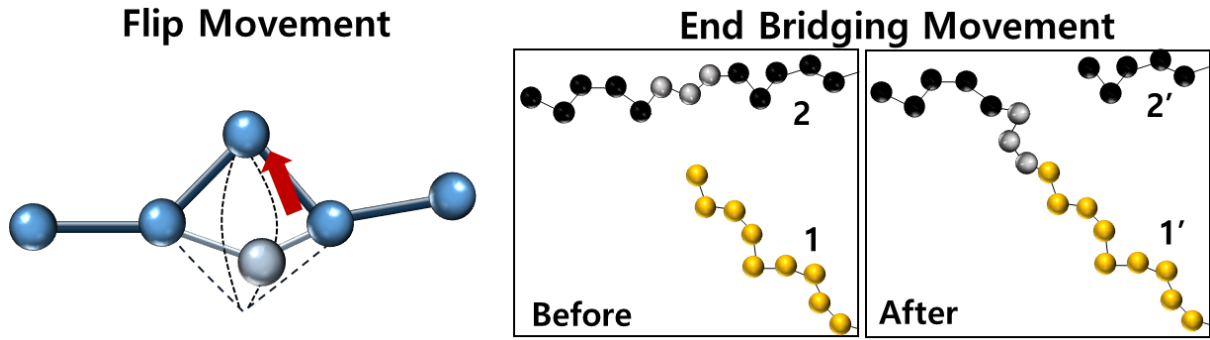
Figure 1.3.2. Schematic illustration for flip movement (left) and end-bridging movement (right).

Regarding the step three, the decision of acceptance or rejection for new polymer configuration is made by comparing the potential energy and some other properties of existing old state and new state. Specifically, the new polymer configuration is welcomed when its potential energy is lower than old one. Otherwise, the proposed sampling is accepted when the acceptance probability P_{acc} consisting of the potential energy difference between two configurations is smaller than the randomly generated number.

For instance, MC simulation at the semi-grand statistical ensemble $\{N_{ch}NVT\mu^*\}$ has the fixed variables: the number of polymer chains N_{ch}, the average number of atoms per chain N, the system volume V, the temperature T, and the spectrum of chain relative chemical potentials μ^* controlling the distribution of chain lengths. The corresponding probability distribution function is given as:

$$\rho^{N_{ch}NVT\mu^*}\left(\mathbf{r}_1,\mathbf{r}_2,...,\mathbf{r}_n,V\right) \sim \exp\left[-\beta\left\{U\left(\mathbf{r}_1,\mathbf{r}_2,...,\mathbf{r}_n,V\right)-\sum_{k=1}^{N_{ch}}\mu_k^*N_k\right\}\right] \qquad (1.3.8)$$

and the Metropolis criterion is

$$P_{acc}^{N_{ch}NVT\mu^*} \sim \exp\left[-\beta\left\{\Delta U-\sum_{k=1}^{N_{ch}}\Delta\left(\mu_k^*N_k\right)\right\}\right] \qquad (1.3.9)$$

where $\beta \equiv 1/k_BT$, n is the total number of atoms in system, μ_k^* the relative chemical potential of the kth chain consisting of N_k atoms.

1.3.3. Simulation model

  The potential function of a system can be divided into the potential energy terms of atoms, pairs, triplets, and etc.

$$U = \sum_{i}^{N} U_1(\mathbf{r}_i) + \sum_{i}^{N}\sum_{j}^{N} U_2(\mathbf{r}_i,\mathbf{r}_j) + \sum_{i}^{N}\sum_{j}^{N}\sum_{k}^{N} U_3(\mathbf{r}_i,\mathbf{r}_j,\mathbf{r}_k) + \cdots \qquad (1.3.10)$$

The first term U_1 in eqn (1.3.9) expresses the external field effects on the system such as flow field, gravity field. The second pair potential energy U_2 is a function of pair separation distance and the most significant interaction in polymeric liquids. And three-body interactions are so time-consuming in calculation and average of the interactions are rarely effective in liquid systems that triplet interactions are usually omitted. The potential interaction can be approximated as pairwise interaction and can be expressed as follows:

$$U = U_{str} + U_{ben} + U_{tor} + U_{LJ} \qquad (1.3.11)$$

The nonbonded intermolecular and intramolecular interactions between atomic units are described by 6-12 Lennard-Jones (LJ) potential.

$$U_{LJ} = 4\varepsilon_{ij}\left[\left(\frac{\sigma_{ij}}{r_{ij}}\right)^6 - \left(\frac{\sigma_{ij}}{r_{ij}}\right)^{12}\right] \qquad (1.3.11)$$

where $\varepsilon_{ij} = \sqrt{\varepsilon_i \varepsilon_j}$ and $\sigma_{ij} = (\sigma_i + \sigma_j)/2$ for cross interactions between atoms i and j by adopting the standard Lorentz-Berthelot mixing rules. The LJ energy parameters ε_{CH_2}/k_B and ε_{CH_3}/k_B were set equal to 47 K and 114 K, respectively, and the size parameters σ_{CH_2} and σ_{CH_3} equal to 3.93 Å identically for SKS potential model. [37] In TraPPE model [38], the LJ energy parameters ε_{CH}/k_B, ε_{CH_2}/k_B, and ε_{CH_3}/k_B were set equal to 10 K, 46 K, and 98 K, respectively, and the size parameters σ_{CH}, σ_{CH_2}, and σ_{CH_3} equal to 4.68 Å, 3.95 Å, and 3.75 Å, respectively. A cut-off distance equal to $2.5\,\sigma_{CH_2}$ was used in all the NEMD simulations. The intramolecular LJ interaction was active only between atoms separated by more than three bonds along the chain. The three bonded interactions [bond-stretching (U_{str}), bond-bending (U_{ben}), and bond-torsional (U_{tor}) energies] were modeled by the following expressions:

$$U_{str}(l) = \frac{k_{str}}{2}(l - l_{eq})^2 \qquad (1.3.12)$$

$$U_{ben}(\theta) = \frac{k_{ben}}{2}(\theta - \theta_{eq})^2 \tag{1.3.13}$$

$$U_{tor}(\phi) = \sum_{m=0}^{3} a_m \cos^m \phi \tag{1.3.14}$$

where the bond-stretching constant and equilibrium bond length were $k_{str}/k_B = 452{,}900$ K/Å^2 and $l_{eq}=$ 1.54 Å, respectively. The bond-bending constant were set as $k_{ben}/k_B = 62{,}500$ K/rad^2, and the equilibrium bending angle $\theta_{eq} = 114°$ for CH$_x$-CH$_2$-CHa$_y$ and $\theta_{eq} = 112°$ for CH$_x$-CH-CH$_y$. The bond-torsional constants were such that (a) $a_0/k_B = 1010$ K, $a_1/k_B = 2019$ K, $a_2/k_B = 136.4$ K, and $a_3/k_B = -3165$ K for CH$_x$-CH$_2$- CH$_2$-CH$_y$, and (b) $a_0/k_B = 395.24$ K, $a_1/k_B = 895.08$ K, $a_2/k_B = 223.7$ K, and $a_3/k_B = -1765.08$ K for CH$_x$-CH$_2$- CH-CH$_y$. Note that $\phi = 0$ represents the (most stable) *trans*-state.

1.4. References

(1) P.G. de Gennes, *J. Chem. Phys.* 1971, **55**, 572–579.

(2) M. Doi and S.F. Edwards, *The Theory of Polymer Dynamics*, 1st ed., Oxford University Press, New York, 1986.

(3) T.C.B. McLeish and R.G. Larson, *J. Rheol.* 1998, **42**, 81–110.

(4) T.C.B. McLeish, J. Allgaier, D.K. Bick, G. Bishko, P. Biswas, R. Blackwell, B. Blottière, N. Clarke, B. Gibbs, D.J. Groves, A. Hakiki, R.K. Heenan, J.M. Johnson, R. Kant, D.J. Read, and R.N. Yong, *Macromolecules* 1999, **32**, 6734–6758.

(5) J.M. Kim, C. Baig, *J. Chem. Phys.* 2016, **144**, 081101

(6) S.H. Jeong, J.M. Kim, C. Baig, *Macromolecules*, 2017, **50**, 4491-4500.

(7) S.H. Jeong, J.M. Kim, C. Baig, *J. Rheol.*, 2018, **62**, 1115-1124.

(8) S. Jeong, J.M. Kim, S. Cho, C. Baig, *Soft Matter*, 2017, **13**, 8644-8650.

(9) M. P. Allen and D. J. Tildesley, *Computer Simulation of Liquids,* Clarendon Press, New York, 1987.

(10) M. Grmela and H. C. Öttinger, *Phys. Rev. E* 1997, **56**, 6620-6632.

(11) H. C. Öttinger and M. Grmela, *Phys. Rev. E* 1997, **56**, 6633-6655.

(12) V. G. Mavrantzas and D. N. Theodorou, *Macromolecules* 1998, **31**, 6310-6332.

(13) V. G. Mavrantzas and H. C. Öttinger, *Macromolecules* 2002, **35**, 960-975.

(14) H. C. Öttinger, *Beyond Equilibrium Thermodynamics,* John Wiley & Sons, New Jersey, 2005.

(15) G. Tsolou, N. Stratikis, C. Baig, P.S. Stephanou, and V.G. Mavrantzas, Macromolecules, 2010, **43**, 10692-10713.

(16) H. Watanabe, T. Inoue, and Y. Matsumiya, *Macromolecules* **39**, 2006, 5419-5426.

(17) R.B. Birds, C.F. Curtiss, R.C. Armstrong, O. Hassager, *Dynamics of Polymer Liquids, Fluid Mechanics*, 2nd ed, John Wiley & Sons, New York, 1987.

(18) F.A. Morrison, *Understanding Rheology*, Oxford University Express, New York, 2001.

(19) E.J. Roh, J.M. Kim, and C. Baig, *Polymer* 2019, **175**, 107-117.

(20) E.J. Roh and C. Baig, *Soft Matter* 2019, **15**, 5271-5281.

(21) S. H.Jeong, S. Cho, E.J. Roh, T.Y. Ha, J.M. Kim, and C.Baig (submitted)

(22) C. Baig, B. J. Edwards, D. J. Keffer and H. D. Cochran, *J. Chem. Phys.* 2006, **124**, 084902.

(23) S. Nosé, *Mol. Phys.* 1984, **52**, 255-268.

(24) W.G. Hoover, *Phys. Rev. A* 1985, **31**, 1695-1697.

(25) M. Tuckerman, B.J. Berne and G.J. Martyna, *J. Chem. Phys.* 1992, **97**, 1990-2001.

(26) V.G. Mavrantzas and D.N. Theodorou, Macromol. *Theory Simul.* 2000, **9**, 500-515.

(27) C. Baig, B.J. Edwards, D.J. Keffer, H.D. Cochran and V.A. Harmandaris, *J. Chem. Phys.* 2006,

124, 084902.

(28) C. Baig and V. G. Mavrantzas, *Phys. Rev. Lett.* 2007, **99**, 257801.

(29) O.Alexiadis, K.Ch. Daoulas and V.G. Mavrantzas, *J. Phys. Chem. B* 2008, **112**, 1198-1211.

(30) C. Baig and V. G. Mavrantzas, *Phys. Rev. B* 2009, **79**, 144302.

(31) C. Baig, O. Alexiadis, and V.G. Mavrantzas, *Macromolecules* 2010, **43**, 986-1002.

(32) K. Moorthi, K. Kamio, J. Ramos and D.N. Theodorou, *Macromolecules* 2012, **45**, 8453- 8466.

(33) S.H. Jeong, J.M. Kim, J. Yoon, C. Tzoumanekas, M. Kröger and C. Baig, *Soft Matter* 2016, **12**, 3770-3786.

(34) P.V.K. Pant and D.N. Theodorou, *Macromolecules*, 1995, **28**, 7224-7234.

(35) G. Mavrantzas, T.D. Boone, E. Zervopoulou and D.N. Theodorou, *Macromolecules*, 1999, **32**, 5072-5096.

(36) N.C. Karayiannis, A.E. Giannousaki, V.G. Mavrantzas and D.N. Theodorou, *J. Chem. Phys.* 2002, **117**, 5465-5479.

(37) J.I. Siepmann, S. Karaborni and B. Smit, *Nature* 1993, **365**, 330-332.

(38) M.G. Martin, J.I. Siepmann, *J. Phys. Chem. B*, 1999, **103**, 4508-4517.

Chapter 2. Intrinsic surface characteristics and dynamic mechanisms of ring polymer

2.1. Introduction

While architecturally characterized as a linear polymer, ring polymers exhibit distinctive structural and dynamical properties [1–4]. It is generally known that ring polymers have relatively compact structures compared with their corresponding linear analogs [3, 5-9]. Typically, pure ring melts exhibit a smaller viscosity, larger diffusion coefficient, and faster relaxation behavior than their corresponding linear analogs. These structural and dynamical behaviors have also been supported by several theoretical analyses, such as the Flory-like mean-field approach, lattice animal model, and crumpled globule model [10-15].

Recent NEMD study on bulk and confined ring melts undergoing steady shear flow found that ring polymers possess strong structural resistance against external flow field and weak interfacial slip in the weak-to-intermediate flow regime compared with linear analog [16]. Other numerical studies have reported dynamical mechanisms for ring chains, such as tank-treading dynamics [17-20] and mutual threading dynamics [21,22].

The distinctive features of ring polymers essentially originate from the intrinsic geometrical constraints of the closed-loop ring topology. Despite extensive efforts of experimental and computational studies, the general structural characteristics and dynamic mechanisms of ring polymers under flow have not yet been fully understood. In this study, we aim to comprehensively analyze the fundamental structural and dynamical features of ring polymers under steady shear flow. To this end, we conducted atomistic NEMD simulations of ring melts and coarse-grained Brownian dynamics (BD) simulations of dilute ring solutions undergoing steady shear flow.

2.2. Simulation methods and Materials studied

We performed detailed atomistic NEMD simulations of ring melts and coarse-grained Brownian dynamics (BD) simulations of dilute ring solutions undergoing steady shear flow. A strictly monodisperse $C_{400}H_{800}$ (unconcatenated and unknotted) ring polyethylene (PE) melt system was employed for the NEMD simulations, which were performed at a constant temperature $T = 450K$ and density $\rho = 0.764$ g cm^{-3} (corresponding to a pressure $P = 1$ atm). A dilute ring solution system devoid of intermolecular interactions was investigated via coarse-grained BD simulations [including the excluded volume (EV) and hydrodynamic interaction (HI) effects] for a bead-rod chain containing 66 beads connected by rigid rods [23]. According to a previous study [24], one rod approximately corresponds to 6 CH_2 monomers for PE molecules in shear flow, thus the bead-rod ring chain roughly matches $C_{400}H_{800}$. A detailed comparison between the ring melt and the dilute ring systems provides useful information to predict the structural and dynamical characteristics of semi-dilute polymer solutions with respect to the polymer concentration.

2.3. Results and Discussion

Considering the closed molecular geometry of ring polymer, we begin the analysis with new viewpoint that ring polymers intrinsically has two-dimensional surface characteristics. Figure. 2.3.1 demonstrates how the simple algorithm allows for the extraction of the characteristic surfaces of the ring chains. Specifically, (i) we start to construct all the non-overlapping local triangular planes, each of which are constituted by three consecutive neighboring atoms (or beads) along the ring backbone; these triangles effectively depict the outermost ring surface. (ii)-(iv) We then apply the same procedure to successively build the inner surfaces of the ring in a step-by-step manner by forming new triangles with the remaining active atoms until only three atoms remained at the end to form the last triangle. This simple algorithm was numerically fast and could properly represent a variety of geometrically complex surfaces formed by ring polymers, as shown in snapshot of Fig. 2.3.1 From the constructed ring surface, we propose the average normal vector $\mathbf{n}_{\text{avg}}$ of the entire surface as a useful physical measure that can effectively characterize the global orientation of a ring chain. For the linear polymers, chain end-to-end vector

$$\mathbf{R}_{\text{ete}} = \sum_{i=1}^{N_b} \mathbf{r}_i = N_b \left(\sum_{i=1}^{N_b} \mathbf{r}_i \Big/ N_b \right)$$ with each bond vector $\mathbf{r}_i$ and total number of local bonds N_b represents

the average bond orientation vector for the whole one-dimensional linear chain . In line with this, by exploiting each surface normal vector $\mathbf{n}_i = \mathbf{r}'_{ia} \times \mathbf{r}'_{ib}$ for two bond vectors consisting a triangle, $\mathbf{n}_{\text{avg}}$

defined as $\mathbf{n}_{\text{avg}} = \sum_{i=1}^{N_s} \mathbf{n}_i = N_s \left(\sum_{i=1}^{N_s} \mathbf{n}_i \Big/ N_s \right)$ represents the average surface orientation vector for the

entire two-dimensional surface formed by a ring topology. Therefore, the $\mathbf{n}_{\text{avg}}$ of the ring polymer is considered to intrinsically correspond with $\mathbf{R}_{\text{ete}}$ for the linear polymer. We demonstrate that these surface properties are very useful for analyzing the fundamental structural and dynamical characteristics of ring polymers under flow conditions.
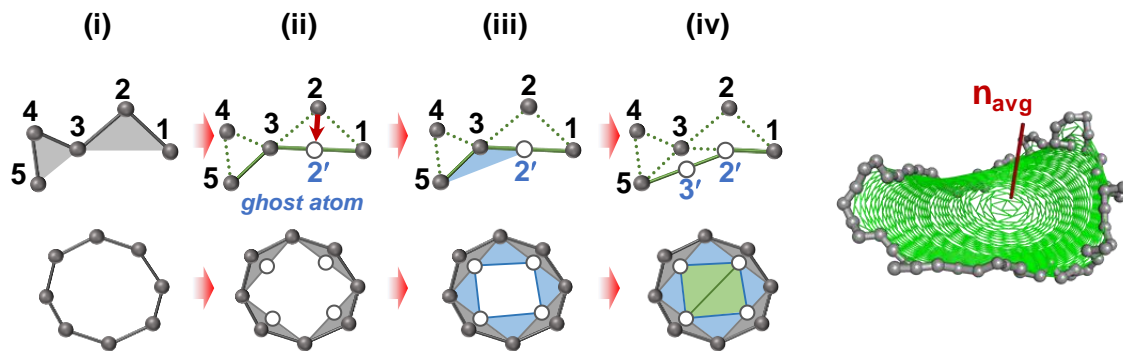
Figure 2.3.1. Schematic description of the numerical algorithm for constructing intrinsic ring surface.

Next, we analyze the basic structural characteristics of the surface orientation and stretch for ring systems under shear flow. For an in-depth understanding of the fundamental aspects of actual ring polymers, we first set up a simple 'toy model' with a fixed two-dimensional square surface by constructing free-draining bead-rod BD simulations without excluded volume effects and hydrodynamic interactions. Results in Fig. 2.3.2 clearly show that the rigid surface tends to lie down preferentially in the *xz*-plane which is the most stable position of the two-dimensional surface, except for certain special initial surface orientations. While the geometric surface formed by the actual flexible ring polymers is generally curved and much more complex, their fundamental orientational characteristics are considered to be essentially similar to those of the aforementioned rigid structure.
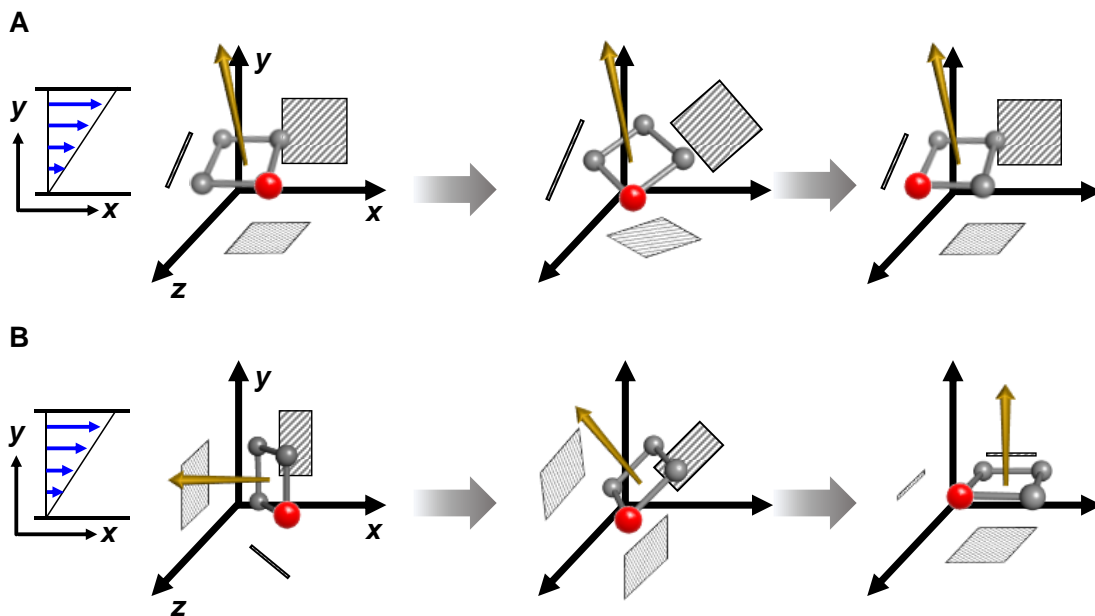
Figure 2.3.2. Rotational illustrations of the toy model under shear flow without the Brownian random force. (A) When there is no surface area facing the *yz*-plane at the initial state. (B) When there is non-zero surface area facing the *yz*-plane at the initial state. The yellow arrows in the illustrations indicate the normal vector of the toy model.

It was confirmed by the results in Fig. 2.3.3 for the projected areas of the curved ring surface for each system, i.e., A_{xy} on the xy-plane, A_{yz} on the yz-plane, and A_{xz} on the xz-plane. We analyzed each projected area normalized by A_t in comparison with the toy model. Notably, both the dilute and melt ring systems exhibited rapid overall increasing and decreasing behaviors for $\langle A_{xz}/A_t \rangle$ and $\langle A_{xy}/A_t \rangle$, respectively, as the flow strength increased. This fully consistent behavior between actual ring polymers and toy model indicates the essentially same fundamental characteristics of the ring surface under shear flow. However, the degree of variation with flow strength appears to be somewhat smaller for actual systems than the toy model. It can be attributed that in real systems, local surface fluctuations are developed in association with many local loops that protrude in the flow-gradient (y)-direction along their flexible backbone. We further notice a larger $\langle A_{xy} / A_t \rangle$ and smaller $\langle A_{yz} / A_t \rangle$ for the ring melt compared with the dilute ring system in the intermediate-to-strong flow regime. This can be closely associated with the higher degree of ring polymer center-loop tumbling dynamics (via strong intermolecular collisions) in the melt relative to a dilute solution; this will be further discussed in the following results. The significant dynamic role of local loops in actual ring polymers can be further confirmed by comparing the $\langle A_{xy} \rangle / \langle A_{xz} \rangle$ in Fig. 2.3.3 representing the degree of surface orientation to the kinematically stable xz-plane under shear flow. While both the dilute and melt systems show consistency in decreasing behavior with increasing shear rate, the degree of change is weaker compared to toy model due to the creation of local loops.
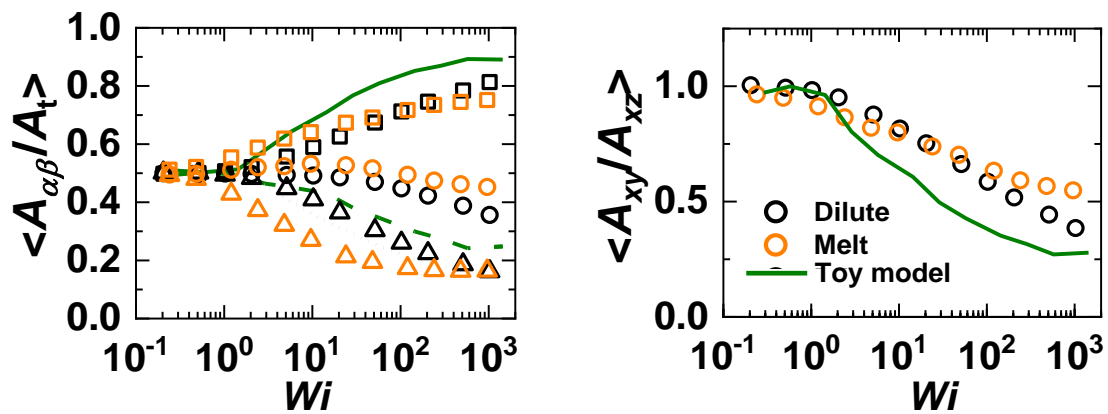
Figure 2.3.3. (Left) Area projected from the intrinsic surface of the ring into three xy- (circles and dashed line), xz- (squares and solid line), and yz- (triangles and dotted line) planes for melt (orange symbols), dilute (black symbols), and toy model (dark green lines) as a function of Weissenberg number (Wi). Note that these projected areas were normalized by the total area of the intrinsic ring surface A_t. (Right) The ratio between A_{xy} and A_{xz} vs. Wi for melt (orange circles), dilute (black circles), and toy model (dark green line).

Figure 2.3.4 shows the characteristic rotational and tumbling dynamics mechanisms of ring chains under shear flow. We note that these primary mechanisms are common to both dilute and melt systems, although the relative proportion of each mechanism with respect to the flow strength is quantitatively different between the two systems, as discussed later. While the chain ends have a dominant role in initiating the rotational and tumbling dynamics in linear polymers, the local loops protruding along the closed ring backbone play a crucial role in activating the dynamic mechanisms in ring polymers. It is noted that short- or long-lived loops can be locally and randomly created via Brownian thermal motion, applied flow field, and intermolecular collisions. In the intermediate flow regime, local loops protruding in the flow-gradient (y-)direction tend to propagate along the closed ring surface boundary (loop-migration) and/or move in space (loop-tumbling) with the flow field. For the loop-migration mechanism, the overall surface structure of the ring is maintained quite well; hence, $\mathbf{n}_{avg}$ is practically unchanged. This means that $\mathbf{n}_{avg}$ does not detect the loop-migration dynamics and this characteristic can be used to distinguish between the loop-migration and loop-tumbling mechanisms for ring rotation. For the loop-tumbling dynamics, ring polymers exhibit two distinct mechanisms: end-loop and center-loop tumbling. The end-loop (S-shaped or hairpin-like) tumbling mechanism of the stretched rings along the flow direction is essentially similar to the typical end-over-end tumbling mechanism for linear chains. However, from a geometrical viewpoint, the former characterizes the overall surface dynamics, while the latter represents the whole line dynamics. Importantly, ring polymers reveal an additional tumbling mechanism driven by the loops located in the middle of the stretched ring backbone. In contrast with the end-loop tumbling mechanism where the overall chain rotation occurs exclusively in the xy-plane, the center-loop mechanism has diagonal chain rotation lying through both the xy- and yz-planes. This center-loop driven tumbling leads to a variety of distinctive average and transient structural and dynamical characteristics for ring polymers in shear flow. $\mathbf{n}_{avg}$ can adequately represent both loop-tumbling mechanisms for ring polymers, similarly to $\mathbf{R}_{ete}$ for linear polymers.

A

Loop migration

**End-loop tumbling
(Hairpin-like)**

**End-loop tumbling
(S-shaped)**

**Center-loop tumbling
(Hairpin-like)**

**Center-loop tumbling
(S-shaped)**

B

Loop migration   End-loop tumbling   Center-loop tumbling

- θ_n
- θ_{xy}
- θ_{yz}

Accum. angle (°)

One tumbling cycle
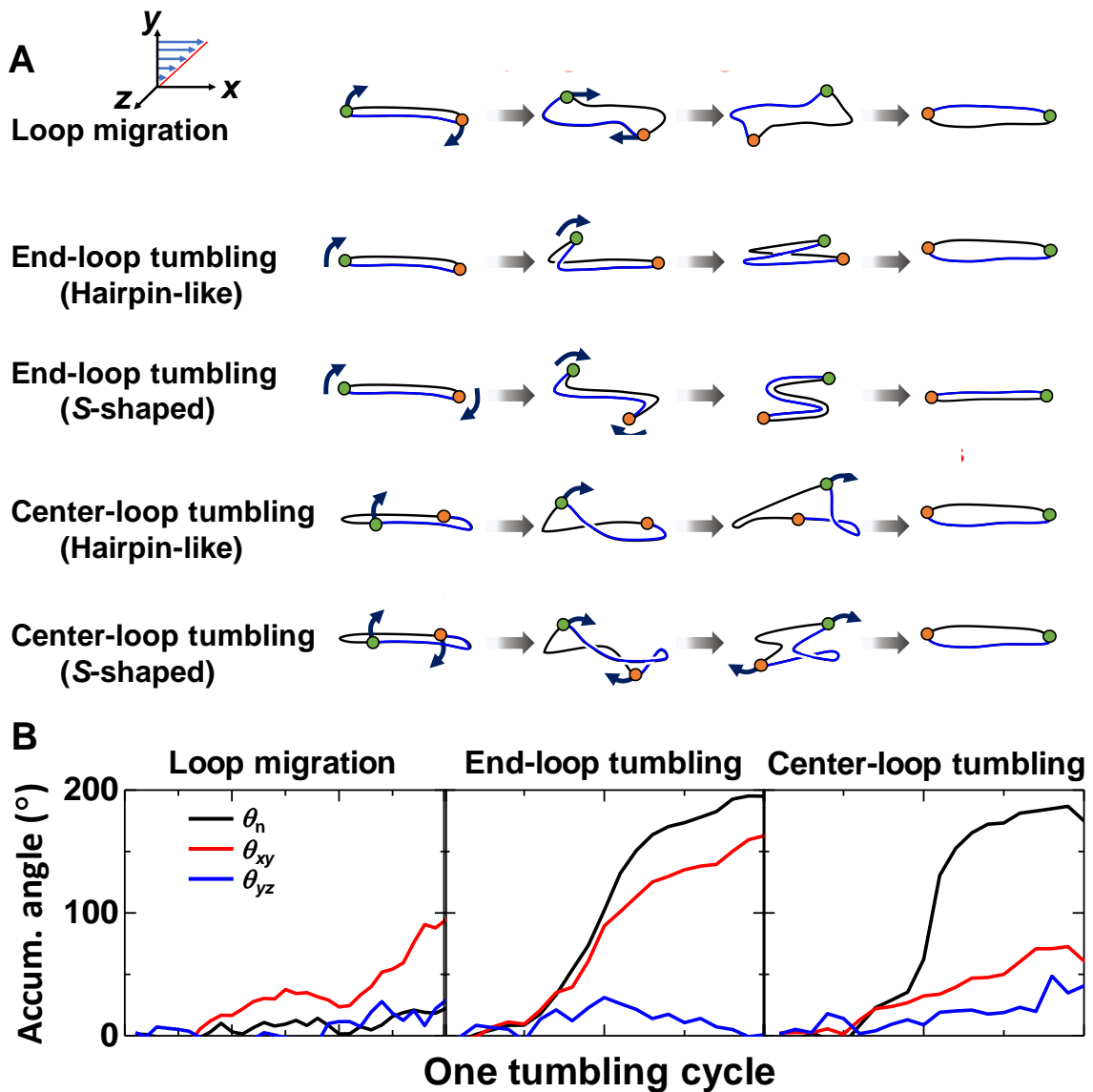
Figure 2.3.4. Molecular mechanisms of ring polymer. (A) Schematic illustrations for the fundamental molecular dynamics mechanisms for the ring polymer under shear flow. (B) Representative results of the average accumulated angle θ_n of $\mathbf{n}_{avg}$, θ_{xy} of $\mathbf{Q}_{xy}$ projected on the xy-plane, and θ_{yz} of $\mathbf{Q}_{yz}$ projected on the yz-plane during loop migration (left panel), end-loop tumbling (middle panel), and center-loop tumbling (right panel).

In Fig. 2.3.4, we illustrate how the representative surface measures such as $\mathbf{n}_{avg}$ and the relative position vectors [$\mathbf{Q}_i = \mathbf{r}_i - \mathbf{r}_c$, for i = 1, 2, …, N_a, where N_a and $\mathbf{r}_c$ are the number of atoms (or beads) per chain and center of mass position vector of a chain, respectively] projected on the xy-plane ($\mathbf{Q}_{xy,i}$) and yz-plane ($\mathbf{Q}_{yz,i}$) can be used to characterize the aforementioned dynamics mechanisms of ring polymers in terms of the angle accumulation during chain rotation and tumbling. The accumulated angle $\theta_n(\Delta t)$ of $\mathbf{n}_{avg}$ is the summation of the angle of $\mathbf{n}_{avg}$ with respect to $\mathbf{n}_{avg}$ at a time origin of t' during $\Delta t = t - t'$. Similarly, the accumulated angle $\theta_{\alpha\beta,i}(\Delta t)$ of $\mathbf{Q}_{\alpha\beta,i}$ projected on the $\alpha\beta$-plane is the summation of angle of $\mathbf{Q}_{\alpha\beta,i}$ with respect to $\mathbf{Q}_{\alpha\beta,i}$ at a time origin of t' during $\Delta t = t - t'$. Thus, $\theta_{\alpha\beta}(\Delta t) = \sum_{i=1}^{N_a} \theta_{\alpha\beta,i}(\Delta t) \Big/ N_a$ with $\alpha, \beta = x$, y, or z represents the average accumulated angle of $\mathbf{Q}_{\alpha\beta,i}$ projected on the $\alpha\beta$-plane. For the loop-migration case, the angles θ_n and θ_{yz} are not accumulated, while θ_{xy} is gradually accumulated indicating mainly xy-plane rotation for loop-migration dynamics. In sharp contrast, for both the end-loop and center-loop tumbling mechanisms, the angle accumulated by $\mathbf{n}_{avg}$ amounts to ~180°, reflecting the upside-down tumbling event for the overall ring surface. Furthermore, θ_{xy} is rapidly accumulated close to 180° for end-loop tumbling, which basically corresponds to the angle of $\mathbf{R}_{ete}$ accumulated during end-over-end tumbling of the linear polymer. In comparison, similarly to each other, θ_{xy} and θ_{yz} are gradually accumulated compared with $\mathbf{n}_{avg}$ for the center-loop tumbling mechanism. Therefore, we can classify the characteristic rotation and tumbling mechanisms of ring polymers with proper analysis on these geometrical surface measures.

Furthermore, in Fig. 2.3.5 we quantified the relative populations of the end-loop tumbling and center-loop tumbling mechanisms for the dilute and melt systems. In the whole flow regime, center-loop tumbling frequently appears than end-loop tumbling for both systems, indicating the significant role of local loops for the ring polymer. However, the melt system shows a particularly higher proportion of the center-loop mechanism due to a significantly high number of loops along the ring backbone created by strong intermolecular interactions. This result implies that the relative portion of center-loop tumbling over that of end-loop tumbling would generally increase with increasing polymer concentration for semi-dilute ring systems. As the flow strength increases, the portion of the end-loop and center-loop mechanisms generally increases and decreases, respectively, for both systems. This change is mainly because the higher chain stretching and alignment in the applied flow direction reduces both the amount and magnitude of local loops.
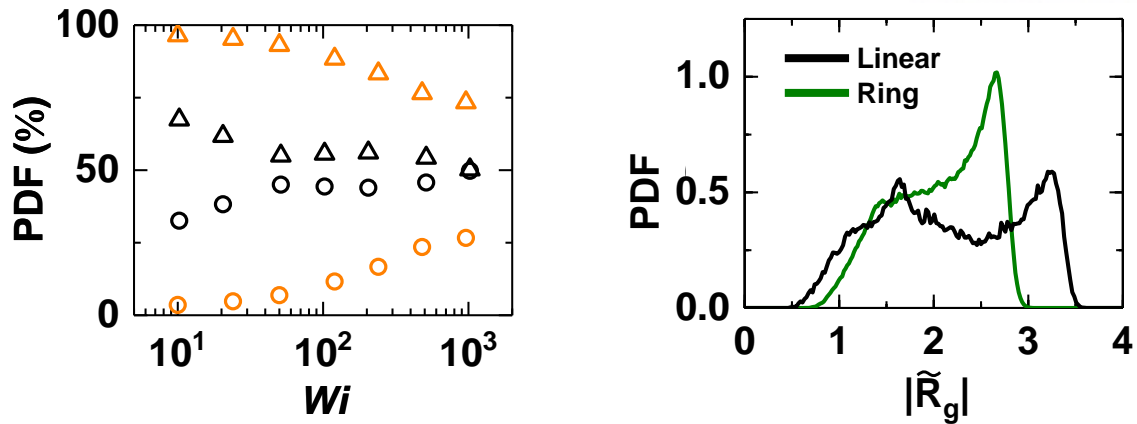
Figure 2.3.5 (Left) The proportion of the end-loop tumbling (circles) and center-loop tumbling (triangles) mechanisms as a function of Wi for the dilute (black) and melt (orange) ring systems. (Right) Probability distribution function (PDF) of the chain radius of gyration normalized by the equilibrium value for the ring (black line) and linear (dark green line) PE melts in the strong flow regime at $Wi = 100$ and 2000, respectively.

Notably, the dilute system shows a rather steep decrease followed by a plateau in the intermediate-to-strong flow regime, indicating somewhat fast saturation of the loop characteristics along with overall chain stretching and orientation. In comparison, the melt system exhibits a gradual decrease of center-loop tumbling in the intermediate flow regime and relatively faster decrease in the strong flow regime. It should be noted that center-loop tumbling is still dominant over end-loop tumbling for the melt system, even at strong flow fields because of many activated local loops formed via strong intermolecular collisions. Furthermore, the hairpin-like end-loop tumbling dynamics become dominant over the *S*-shaped one in the strong flow regime for both dilute and melt systems, similar to linear polymers [25-28]. This dynamical feature of ring polymer directly affects the overall shape of the probability distribution $P(R_g)$ of the chain radius of gyration (R_g). Because stretched ring structures can be maintained during center-loop tumbling dynamics without the compact folded conformation that occurs during the end-loop tumbling dynamics (which is similar to the end-over-end tumbling dynamics of linear polymer), ring melt is supposed to exhibit a weaker rotation peak and relatively larger stretched portions in $P(R_g)$ compared with the linear analog, which is evident in Fig. 3*B*.

2.4. Conclusion

In conclusion, we conducted a comprehensive study on the intrinsic structural characteristics and dynamic mechanisms of ring polymers under shear flow with both dilute and melt conditions. Our analysis began with the new viewpoint that ring polymers intrinsically possess two-dimensional surface characteristics because of their closed-loop geometry, which is in contrast with the one-dimensional line characteristics of linear polymers. Based on this view, we introduced several representative physical measures that could effectively describe the structural and dynamical characteristics of ring polymers, such as the total and projected surface areas and the average normal vector $\mathbf{n}_{avg}$ of the ring surface, which was found to be very informative for analyzing the characteristic molecular dynamics mechanisms of ring chains.

An efficient numerical scheme was also developed that allowed us to effectively describe the complex curved surface formed by flexible ring chains. The obtained surface information was found to be very useful for analyzing the characteristic dynamic mechanisms of ring polymers under shear flow.

The new curved surface criteria and categorization of the ring-polymer dynamics proposed in this work can serve as fundamental descriptors for analyzing various ring-shaped polymers and systems, such as branched ring polymers, ring-shaped biological molecules, and two-dimensional polymers.

2.5. Reference

(1) M. Kapnistos, M. Lang, D. Vlassopoulos, W. Pyckhout-Hintzen, D. Richter, D. Cho, T. Chang, and M. Rubinstein, *Nat. Mater*. 2008, **7**, 997-1002.

(2) J. Roovers, *Macromolecules* 1985, **18**, 1359-1361.

(3) J. D. Halverson, W. B. Lee, G. S. Grest, A. Y. Grosberg, K. Kremer, *J. Chem. Phys*. 2011, **134**, 204904.

(4) R. Pasquino, T. C. Vasilakopoulos, Y. C. Jeong, H. Lee, S. Rogers, G. Sakellariou, J. Allgaier, A. Takano, A. R. Brás, T. Chang, S. Gooßen, W. Pyckhout-Hintzen, A. Wischnewski, N. Hadjichristidis, D. Richter, M. Rubinstein, and D. Vlassopoulos, *ACS Macro Lett*. 2013, **2**, 874-878.

(5) S. Brown, T. Lenczycki, and G. Szamel, *Phys. Rev. E* 2001, **63**, 052801.

(6) V. Arrighi, S. Gagliardi, A. C. Dagger, J. A. Semlyen, J. S. Higgins, and M. J. Shenton, *Macromolecules* 2004, **37**, 8057-8065.

(7) G. Tsolou, N. Stratikis, C. Baig, P. S. Stephanou, and V. G. Mavrantzas, *Macromolecules* 2010, **43**, 10692-10713.

(8) T. Vettorel, A. Y. Grosberg, and K. Kremer, *Phys. Biol*. 2009, **6**, 025013.

(9) A. Rosa and R. Everaers, *Phys. Rev. Lett*. 2014, **112**, 118302.

(10) M. E. Cates and J. M. Deutsch, *J. Phys. (France)* 1986, **47**, 2121-2128.

(11) T. Sakaue, *Phys. Rev. E* 2012, **85**, 021806.

(12) S. P. Obukhov, M. Rubinstein and T. Duke, *Phys. Rev. Lett*. 1994, **73**, 1263.

(13) S. T. Milner and J. D. Newhall, *Phys. Rev. Lett*. 2010, **105**, 208302.

(14) A. Y. Grosberg, S. K. Nechaev, and E. I. Shakhnovich, *J. Phys. (France)* 1988, **49**, 2095-2100.

(15) J. Yoon, J. Kim, and C. Baig, *J. Rheol*. 2016, **60**, 673-685.

(16) S. Jeong, S. Cho, J. M. Kim, and C. Baig, *Macromolecules* 2018, **51**, 4670-4677.

(17) A. J. Tsamopoulos, A. F. Katsarou, D. G. Tsalikis, and V. G. Mavrantzas, *Polymers* 2019, **11**, 1194.

(18) K. W. Hsiao, C. M. Schroeder, and C. E. Sing, *Macromolecules* 2016, **49**, 1961-1971.

(19) C. D. Young, J. R. Qian, M. Marvin, and C. E. Sing, *Phys. Rev. E* 2019, **99**, 062502.

(20) W. Chen, J. Chen, and L. An, *Soft Matter* 2013, **9**, 4312-4318.

(21) D. G. Tsalikis, V. G. Mavrantzas, and D. Vlassopoulos, *ACS Macro Lett*. 2016, **5**, 755-760.

(22) J. Smrek, K. Kremer, and A. Rosa, *ACS Macro Lett*. 2019, **8**, 155-160.

(23) H. C. Öttinger, *Phys. Rev. E* 1994, **50**, 2696.

(24) R. Ramachandran G. Beaucage, A. S. Kulkarni, D. McFaddin, J. Merrick-Mack, and V. Galiatsatos, *Macromolecules* 2008, **41**, 9802-9806.

(25) Z. Xu, S. Kim and J. J. de Pablo, *J. Chem. Phys*. 1994, **101**, 5293-5304.

(26) C. M. Schroeder, R. E. Teixeira, E. S. G. Shaqfeh, and S. Chu, *Phys. Rev. Lett.* 2005, **95**, 018301.

(27) R. E. Teixeira, H. P. Babcock, E. S. G. Shaqfeh, and S. Chu, *Macromolecules* 2005, **38**, 581-592.

(28) J. M. Kim, B. J. Edwards, D. J. Keffer, and B. Khomami, *J. Rheol.* 2010, **54**, 283-310.

# Chapter 3. Molecular Dynamics study on the structure and relaxation of short-chain branched ring polymer melts

3.1. Introduction

The numerous research efforts have been made to characterize the distinctive structural and rheological behaviors of polymers with respect to their molecular architectures. Significant advances have been achieved over the past in comprehending the behaviors of linear and long-chain branched (LCB) polymers. For instance, the fundamental characteristics of dynamics of entangled linear and LCB polymers have been well explained by the tube theory originally developed by de Gennes [1] and Doi-Edwards [2], where entanglement effects are effectively accounted for via a mean-field tube and the dynamics is thus assumed to be strictly restricted to such a one-dimensional curvilinear tube region, leading to a snake-like reptative chain motion. Similar dynamical features have been applied to LCB polymers: here, however, each dangling long branch (arm) is supposed to perform a repetitive retractive (breathing) motion starting from its free end all the way down to the fixed branch (or junction) point that is directly connected to the chain backbone [3-5]. In contrast, the fundamental characteristics of short-chain branched (SCB) polymers have not yet been well understood mainly due to the inapplicability of the standard entropic-based approach [3,4] to describe the dynamics of branches whose length is generally too short. Accordingly, the structural and dynamical characteristics of SCB polymers have usually been assumed to be similar to those of linear polymers. However, recent numerical studies [6-9] of unentangled SCB polymer systems have revealed the fundamental role of short branches via their very fast random Brownian movements that gives rise to distinctive structural and dynamical features of SCB polymers. For instance, in comparison to the linear polymers, the SCB polymers exhibit more compact and less deformed chain structures in response to an applied flow, thereby resulting in distinctive rheological behaviors such as a reduced shear-thinning behavior. Another interesting chain molecule is ring polymer, which is characterized as a linear polymer but with internally closed-loop topology without chain ends. Due to the absence of the free chain ends that are necessary for the whole chain reptation or arm relaxation mechanisms, the standard tube theory [1,2] cannot be applied to describe the dynamics of ring polymers. It has been well documented that the intrinsic closed-loop geometry of ring polymer generally leads to a more compact polymer structure, giving rise to substantially distinct structural and rheological characteristics from the linear polymer [10-27]. For example, a recent numerical study of atomistic nonequilibrium molecular dynamics (NEMD) simulations for ring melts under shear and planar elongational flows showed that in comparison to the linear analogues, ring polymers exhibit a much lesser degree of chain stretch and

alignment in response to the applied flow [21]. Yet, there remains an open issue in regard to the characteristic molecular mechanisms (e.g., mutual threading between rings) that underlie distinctive dynamical properties, such as diffusion coefficient and viscosity, for ring melts [22-26]. Considering the unique viscoelastic behaviors of the ring and SCB polymers and their potential benefits in polymer industry, the major objective of this study is to analyze how the short branches influences the local- and large-scale chain structure and intrinsic relaxation behavior for the SCB ring polymers, in conjunction with the close-loop ring geometry and the nonconcatenation topological constraints between ring chains. Here we investigated various structural properties and relaxation characteristics of the SCB ring polymers using atomistic equilibrium molecular dynamics (MD) simulations. Additionally, the results for the SCB ring system were directly compared with those of the SCB linear analogue. To quantify the short-branching effects, results of the SCB linear and ring polymers were further compared with those of the corresponding bare linear and ring polymers having the same backbone length but without short branches.

3.2. Simulation methods and Materials studied

In present work, two short-chain branched polyethylene (PE) molecules were employed: (i) the SCB linear system (denoted as SCB_L_400_33x5) and (ii) the SCB ring system (denoted as SCB_R_400_33x5) where each chain contains 400 carbon atoms in the (linear and ring, respectively) backbone and uniformly distributed 33 short branches along the backbone with each consisting of 5 carbon atoms. Therefore, each chain contains 565 carbon atoms in total for the SCB ring and linear systems. To quantify the short-branching effects systematically, two unbranched polymers were chosen as reference for each of the linear and ring SCB systems, based on the total and the backbone molecular weight; i.e., $C_{400}H_{802}$ and $C_{565}H_{1132}$ linear polymers (denoted by L_400 and L_565, respectively) and $C_{400}H_{800}$ and $C_{565}H_{1130}$ ring polymers (denoted by R_400 and R_565, respectively). Figure 2.2.1 schematically depicts the representative molecular architectures of the linear and ring polymers and the corresponding SCB polymers.
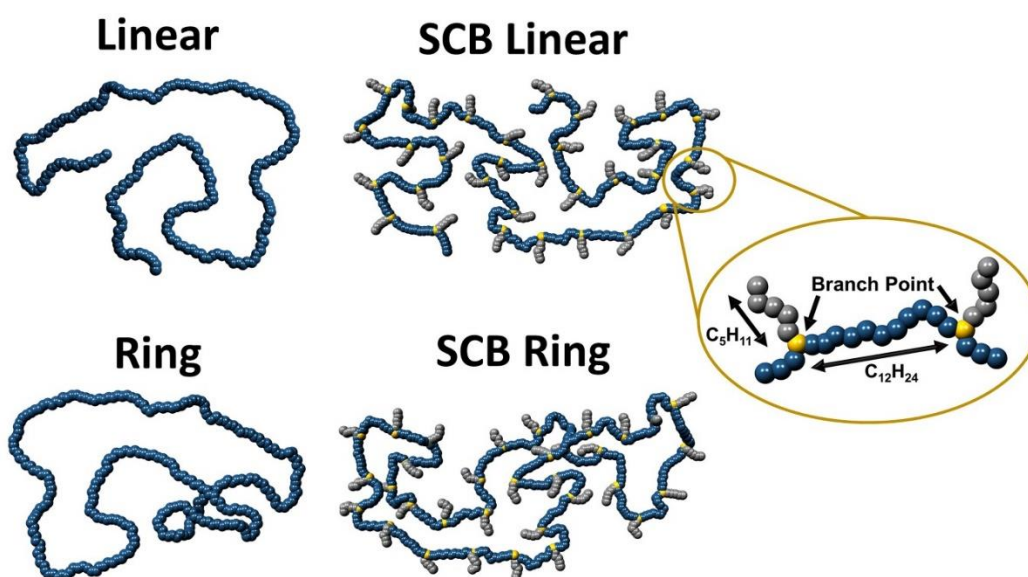
Figure 2.2.1. Schematic image of the molecular architectures for the bare linear (L_400 and L_565) and ring (R_400 and R_565) PE and the short-chain branched linear (SCB_L_400_33x5) and ring (SCB_R_400_33x5) PE systems simulated in this study. The detailed local structure of SCB polymers is depicted in the yellow circle.

The equilibrium MD simulations were conducted for all systems in the isothermal-isobaric (*NPT*) statistical ensemble at constant temperature $T = 450$ K and constant pressure $P = 1$ atm using the Nosé-Hoover thermostat and barostat [28,29]. Each system was enclosed in a cubic simulation box whose initial dimension was set as more than two times the average chain radius of gyration R_g for the system to avoid system-size effects. The average box dimensions for the L_400, L_565, R_400, R_565, SCB_L_400_33x5, and SCB_R_400_33x5 systems were equal to 86.55 Å 105.82 Å, 84.50 Å, 100.23 Å, 97.05 Å, and 96.98 Å, respectively. The set of the evolution equations was numerically integrated using reversible reference system propagation algorithm (*r*-RESPA) [30] with two different time scales in an MD step: 0.48 fs for the bond-stretching, bond-bending, and bond-torsional interactions, and 2.39 fs for the nonbonded inter- and intramolecular Lennard-Jones (LJ) interactions and the Nosé-Hoover thermostat and barostat. The well-known Transferable Potentials for Phase Equilibria (TraPPE) united atom potential model [31] was adopted for all the systems, with the exception that the rigid bond assumed in the original model was replaced by a flexible one with a harmonic potential and a relatively large spring constant.

3.3. Results and Discussion

The Table 3.3.1 shows the simulation results for the density (ρ), characteristic chain dimensions ($\langle R_d^2 \rangle$, $\langle R_{ete}^2 \rangle$, $\langle R_g^2 \rangle$), packing length (l_p), and eigenvalues (λ_1, λ_2, λ_3) of the gyration tensor for the all PE melt systems. The system density at $T = 450$ K and $P = 1$ atm appears to be slightly larger for the ring melts in comparison to the corresponding linear melts, due to the absence of chain ends and the nonconcatenation topological constraints for ring polymers. In addition, the SCB_R_400_33x5 and SCB_L_400_33x5 systems exhibit a slightly higher density than their bare ring systems without short branches, indicating that the increase in the total free volume space of the system via many short-branch ends is sufficiently compensated by the local structural compactness around each branch point.

Concerning the global-scale chain dimension, $\langle R_{ete}^2 \rangle_{linear} / \langle R_d^2 \rangle_{ring}$ are equal to 2.6 and 3.1 for the $C_{400}H_{802}$ and $C_{565}H_{1130}$, respectively. These values larger than 2 that is predicted by the Rouse model [14] and Zimm and Stockmayer [32] are attributed to the overall compact chain structures via nonconcatenation topological constraints between ring chains imposing an effective pressure on individual rings [10,14-20] (as consistent, the ratio $\langle R_{ete}^2 \rangle_{linear} / \langle R_d^2 \rangle_{ring}$ between the mean-square chain end-to-end distance $\langle R_{ete}^2 \rangle$ and the mean-square ring diameter $\langle R_d^2 \rangle$ is shown to be larger than 4 predicted by the Rouse model [14]). It is noticeable that SCB_L_400_33x5 and SCB_R_400_33x5 systems show the reduced backbone dimensions than linear (L_400) and ring (R_400) systems at the same backbone molecular weight. The relatively compact backbone structures of the SCB polymers are attributed to the inherent Brownian motions of short branches located along the backbone. [6-9].

Table 3.3.1. Results for the density ρ, mean-square ring diameter $\langle R_d^2 \rangle$, mean-square chain end-to-end distance $\langle R_{ete}^2 \rangle$, mean-square chain radius of gyration $\langle R_g^2 \rangle$, packing length l_p, and three principal eigenvalues ($\lambda_1 \geq \lambda_2 \geq \lambda_3$) of gyration tensor $G_{\alpha\beta}$ for the simulated linear, ring, and SCB PE melts. The values in parentheses represent the results based on only the chain backbone for the SCB PE systems.

system	ρ (g/cm³)	$\langle R_d^2 \rangle (\text{Å}^2)$	$\langle R_{ete}^2 \rangle (\text{Å}^2)$	$\langle R_g^2 \rangle (\text{Å}^2)$	$\langle R_g^2 \rangle_{SCB} / \langle R_g^2 \rangle_{C400}$	$\langle \lambda_1 \rangle / \langle \lambda_3 \rangle$	$\langle \lambda_2 \rangle / \langle \lambda_3 \rangle$
R_400	0.7760 ± 0.0004	1468 ± 42	-	504 ± 15	-	7.1 ± 0.8	2.4 ± 0.2
R_565	0.7761 ± 0.0008	1870 ± 51	-	653 ± 17	-	6.5 ± 0.7	2.3 ± 0.1
SCB_R_400_33x5 (backbone)	0.7778 ± 0.0009	1355 ± 36	-	475 ± 13 (460 ± 13)	0.94 ± 0.02 (0.91 ± 0.02)	6.0 ± 0.6 (6.4 ± 0.7)	2.2 ± 0.2 (2.3 ± 0.2)
L_400	0.7744 ± 0.0005	-	8160 ± 240	1335 ± 25	-	13.1 ± 1.8	3.0 ± 0.4
L_565	0.7758 ± 0.0001	-	12251 ± 220	2018 ± 26	-	14.0 ± 1.4	2.9 ± 0.3
SCB_L_400_33x5 (backbone)	0.7770 ± 0.0010	-	7807 ± 139	1270 ± 38 (1255 ± 26)	0.95 ± 0.03 (0.94 ± 0.02)	13.6 ± 1.6 (14.5 ± 1.7)	2.8 ± 0.3 (3.0 ± 0.4)

As demonstrated in recent numerical studies [6-9], fast random movements of short branches constantly disturb the overall chain conformation and lead to a more compact and less deformed chain structure in response to the applied flow. Interestingly, it is seen from the relative ratio of chain radius of gyration $\left\langle R_g{}^2 \right\rangle_{\text{SCB}} / \left\langle R_g{}^2 \right\rangle_{\text{C400}}$ between the SCB polymers (SCB_L_400_33x5 and SCB_R_400_33x5) and the corresponding bare linear (L_400) and ring (R_400) systems in Table 3.3.1 that the degree of structural compactness due to the short branches is quantitatively very similar between the ring and linear SCB polymers. This feature indicates that the dynamical role of the short branches and their influences in determining the structural characteristics remain the same, irrespective of the molecular architectures of polymer.

In addition to the global chain size, we further analyzed the variation in the overall shape of polymer chains in association with the ring topology and the short branches, based on the three eigenvalues ($\lambda_1 \geq \lambda_2 \geq \lambda_3$) of the second-rank chain radius of gyration tensor ($G_{\alpha\beta}$) which represent the spatial distributions of monomers along the three mutually-orthogonal principal directions. All polymer systems exhibit a standard prolate ellipsoidal chain shape, irrespective of their molecular architectures. However, ring polymers, due to their closed-loop geometrical constraint, possess a lesser degree of asymmetry in shape as compared to the linear analogues. Specifically, the R_565 system displays a more symmetrical (spherical) shape than the R_400 system. This is due to a stronger effect of the nonconcatenation topological constraint imposing an effective pressure on chains for longer rings [10,14-20]. Regarding the effect of short branches, in spite of their reduced chain dimension, the SCB linear and SCB ring systems exhibit practically identical chain shape to that of the corresponding bare linear and ring systems, respectively.

To understand the influences of short branches on the local structure, we conducted a detailed analysis on the torsional angle (ϕ) distributions. Figure 3.3.1(a) presents the distribution $P(\phi)$ for the simulated ring, linear, and SCB PE systems. First, the ring and linear polymers either with or without short branches exhibit quantitatively very similar behaviors of $P(\phi)$ to each other in the whole range of ϕ, implying their similar overall chain structures. However, it should be noted that the ring systems possess a slightly higher value (~1%) for the relative ratio of the *gauche*-state to the *trans*-state than the linear systems, as shown in Table 3.3.2, due to the intrinsic closed-loop topology and geometrical constraint (i.e., nonconcatenation).
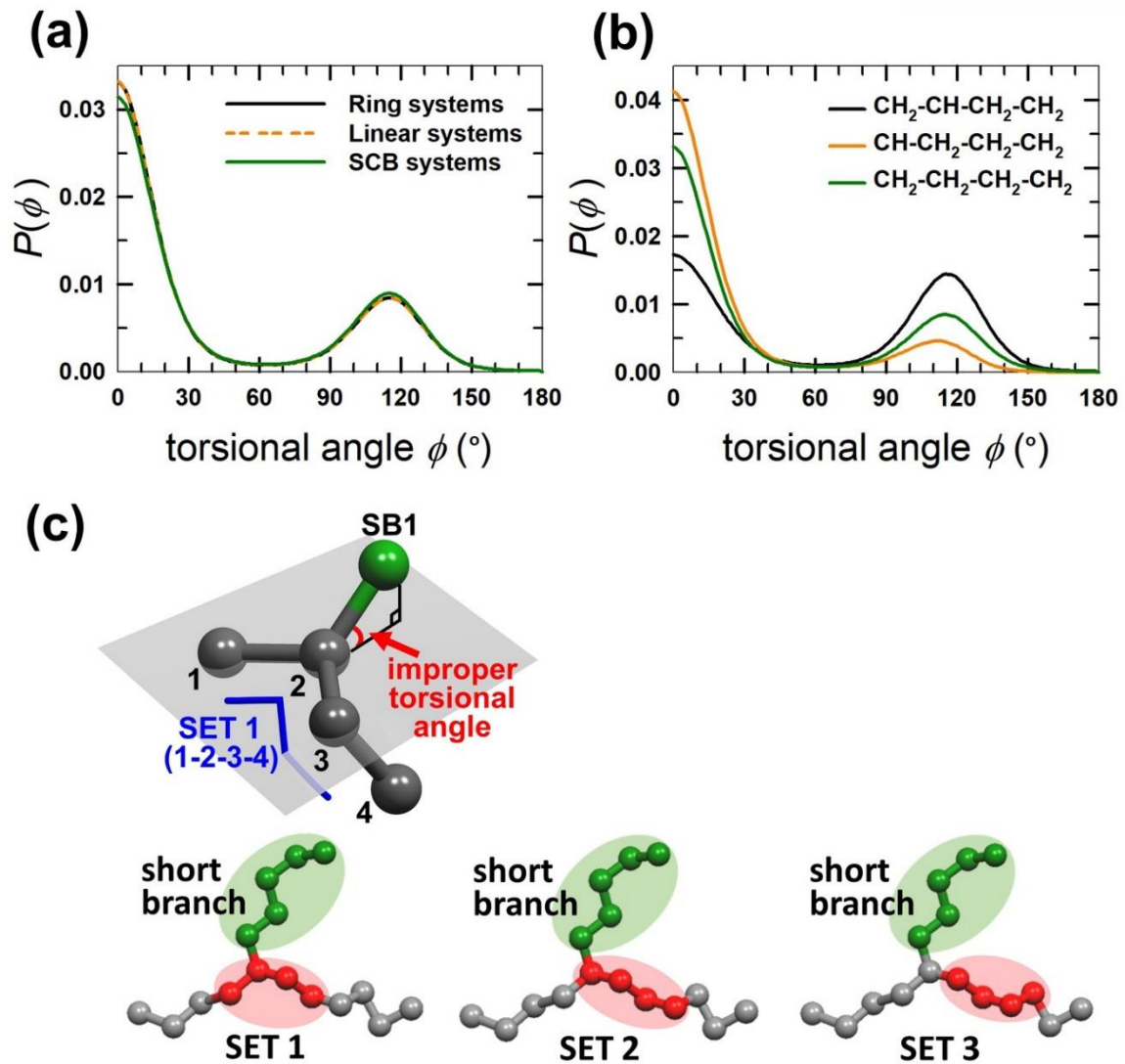
Figure 3.3.1. (a) Probability distribution function $P(\phi)$ of the bond-torsional angle ϕ along the chain backbone. (b) $P(\phi)$ of the three distinct backbone torsional modes [CH_2-CH-CH_2-CH_2 (SET 1), CH-CH_2-CH_2-CH_2 (SET 2), and CH_2-CH_2-CH_2-CH_2 (SET 3)] for the simulated SCB ring (SCB_R_400_33x5) and linear (SCB_L_400_33x5) PE systems. (c) Schematic illustrations for the improper torsional mode constituted by the first CH_2 unit of short branch (denoted by 'SB1') and CH_2-CH-CH_2 (denoted by '1-2-3') in SET 1 around the branch point (top panel) and for the three distinct backbone torsional modes (SET 1, SET 2, and SET 3) (bottom panels) for the simulated SCB PE systems.

Table 3.3.2. Population of the *trans*- and *gauche*-states for the bond-torsional mode along the chain backbone for the simulated ring, linear, and SCB PE systems.

system	*trans* (%)	*gauche* (%)
R_400	65.6 ± 0.2	34.4 ± 0.2
R_565	65.8 ± 0.2	34.2 ± 0.2
L_400	66.5 ± 0.1	33.5 ± 0.1
L_565	66.5 ± 0.3	33.5 ± 0.3
SCB_R_400_33x5 (backbone)	63.8 ± 0.2	36.2 ± 0.2
SET 1 (CH_2-CH-CH_2-CH_2)	41.8 ± 0.3	58.2 ± 0.3
SET 2 (CH-CH_2-CH_2-CH_2)	81.0 ± 0.3	19.0 ± 0.3
SET 3 (CH_2-CH_2-CH_2-CH_2)	65.0 ± 0.1	35.0 ± 0.1
SCB_L_400_33x5 (backbone)	64.5 ± 0.2	35.5 ± 0.2
SET 1 (CH_2-CH-CH_2-CH_2)	42.3 ± 0.1	57.7 ± 0.1
SET 2 (CH-CH_2-CH_2-CH_2)	81.8 ± 0.1	18.2 ± 0.1
SET 3 (CH_2-CH_2-CH_2-CH_2)	65.8 ± 0.1	34.2 ± 0.1

Importantly, in comparison to their corresponding bare systems without short branches, the SCB ring and linear systems exhibit a noticeable quantitative discrepancy, especially with respect to the relative portions between the *trans*- and *gauche*-states (i.e., amounting to ~2% increase for the *gauche*-state and correspondingly ~2% decrease for the *trans*-state). This difference underlies the distinctive large-scale structural characteristics of the SCB systems, as shown in Table 3.3.1. Additionally, the difference in $P(\phi)$ would become more intensified with increasing the branch density, dramatically influencing the overall chain structures and dynamical properties under equilibrium or nonequilibrium (flowing) conditions.

To further understand the torsional differences associated with short-chain branching, we separately analyzed the probability distribution functions of the three distinct backbone torsional modes for the SCB PE melts, i.e., CH_2-CH-CH_2-CH_2 (SET 1), CH-CH_2-CH_2-CH_2 (SET 2), and CH_2-CH_2-CH_2-CH_2 (SET 3). Here, SET 1 and SET 2 are directly involved with the short branches whereas SET 3 is not. As shown in Fig. 3.3.1(b), SET 1 displays a significantly higher extent of the *gauche*-conformation relative to the *trans*-conformation compared to SET 3. This structural feature can be understood by considering the improper torsional mode constituted by the first CH_2 unit of short branch (denoted by 'SB1') and CH_2-CH-CH_2 (denoted by '1-2-3') in SET 1, as schematically illustrated in Fig. 3.3.1(c). Due to the strong bending-angle (θ) constraints (i.e., $\theta \approx 112°$) for each of the three bending modes around the branch point [i.e., 1-2-3, 1-2-SB1, 3-2-SB1 in Fig. 3.3.1(c)], the 'SB1' and '1-2-3' cannot be placed on the same plane. As shown in Fig. 3.3.2, the improper torsional mode exhibits a quite narrow probability distribution with a high peak at $\phi \approx 48°$, indicating a rather stiff local structure around the junction points. Therefore, SET 1 would prefer to have a torsional conformation somewhat skewed from the *trans*-conformation (thereby having a lesser degree of the *trans*-state) in order to avoid a relatively high energy state via a steric overlap between the 'SB1' and the last CH_2 unit in SET 1 [atom '4' in Fig. 3.3.1(c)]. This results in a relative increase in the population of the *gauche*-state of SET 1, with which the torsional mode consisting of the 'SB1' and CH-CH_2-CH_2 (2-3-4) in SET 1 can be approximately close to the *trans*-state. In turn, this higher probability of the *gauche*-state of SET 1 is likely to suppress the amount of the *gauche*-state of SET 2, because of the pentane effect [33] [i.e., two consecutive torsional conformation states of *gauche$^+$*-*gauche$^-$* (or *gauche$^-$*-*gauche$^+$*) being energetically unfavorable], leading to a relative decrease and increase in the population of the *gauche*- and *trans*-conformation states, respectively, for SET 2, as confirmed in Fig. 3.3.1(b) and Table 3.3.2. As SET 3 does not directly involve the short branches, its torsional angle distribution appears to be nearly identical to that of polymer chains without short branches for both ring and linear PE melts.
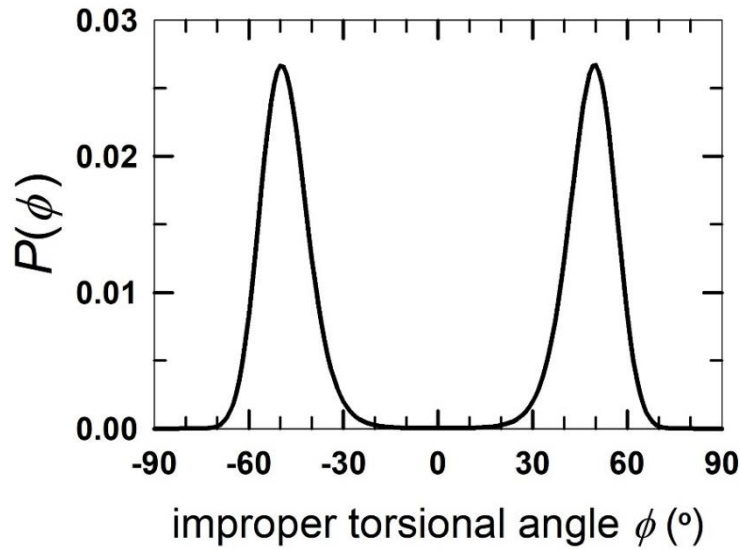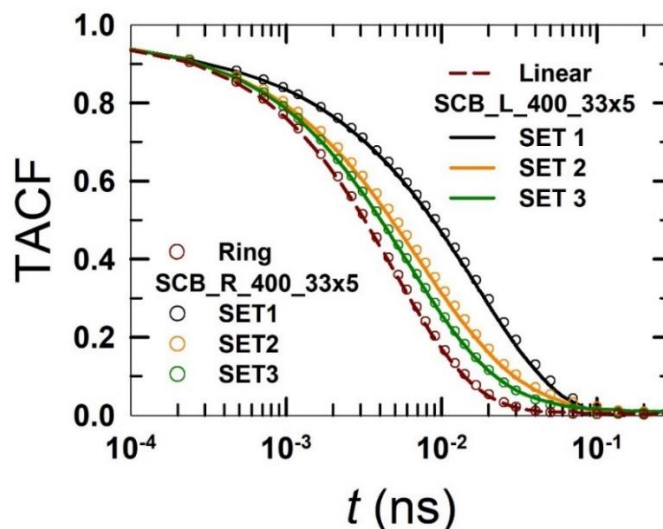
Figure 3.3.2. Probability distribution function $P(\phi)$ of improper torsional angle ϕ around branch point for the SCB (SCB_R_400_33x5 and SCB_L_400_33x5) systems. The SCB ring and linear systems exhibit a quantitatively similar behavior of $P(\phi)$ to each other in the whole range of the improper torsional angle. The positive and negative signs indicate a position of the angle above and below the plane, respectively. The narrow probability distribution with a high peak at $\phi \approx \pm 48°$ indicates a rather stiff local structure around the branch point.

We further analyzed the dynamics of the three torsional modes involved with short branches in comparison to that of the regular torsional mode in the bare linear and ring polymers. In Fig. 2.3.3, we plot the torsional time autocorrelation function (TACF) for the simulated linear, ring, and SCB PE melt systems, which is defined as:

$$\text{TACF}(\phi(t)) = \frac{\langle \cos(\phi(t))\cos(\phi(0))\rangle - \langle \cos(\phi(0))\rangle^2}{\langle \cos(\phi(0))\cos(\phi(0))\rangle - \langle \cos(\phi(0))\rangle^2} \tag{3.3.1}$$

Figure 3.3.3. Torsional time autocorrelation function (TACF) along the chain backbone for the simulated PE systems. For the SCB systems, TACFs for the three different backbone torsional modes [CH_2-CH-CH_2-CH_2 (SET 1, black), CH-CH_2-CH_2-CH_2 (SET 2, yellow), and CH_2-CH_2-CH_2-CH_2 (SET 3, green)] are separately plotted. The bare linear and ring PE systems are represented by 'Linear' and 'Ring', respectively.

We first note that the TACFs for the bare linear and ring systems without short branches appear to be practically indistinguishable, indicating that the local torsional dynamics is irrelevant to the large-scale topological difference (i.e., linear and ring structure) as well as the chain length for sufficiently long polymer molecules. In contrast, the three torsional modes (SET 1, SET 2, and SET 3) for the SCB systems display quantitatively very different behaviors from each other. Specifically, SET 1 and SET 2 that are explicitly involved with the branch point exhibit significantly slower relaxation behaviors compared to SET 3 indicating that the local torsional dynamics can be significantly affected by the short branches, presumably independent of the branch length. As shown in Fig. 3.3.2, these slower dynamics of SET 1 and SET 2 are ascribed to an extra local torsional stiffness imposed by the short branches in conjunction with a rather stiff improper torsional interaction around the branch point. Also noticeable is that SET 3 for the SCB polymers exhibits a relatively slower dynamics in comparison to the regular torsional mode. This is because neighboring torsional modes are not completely independent of each other but have a certain degree of mutual correlation between each other (this correlation is supposed to become stronger with increasing the branch density).

Let us now compare the structural and dynamical characteristics of the Rouse normal modes for the simulated ring, linear, and SCB melt systems. The Rouse normal coordinate is defined as [2,13,14]

$$\mathbf{X}_p(t) = \frac{1}{N}\int_0^N \mathbf{R}_n(t)\cos\left(\frac{p\pi n}{N}\right)dn \qquad (3.3.2)$$

where $\mathbf{R}_n(t)$ represents the position vector of the nth atom along the chain at time t. Here, only the backbone atoms were included in the normal mode analysis for the SCB ring and linear polymers, since the branches are too short (i.e., even below the Kuhn length corresponding to about 11 carbon atoms for PE) to be statistically meaningful in the Rouse mode analysis. In addition, for comparison purpose, the two linear and the SCB linear polymers (L_400, L_565, and SCB_L_400_33x5) are replaced by relatively shorter polymers such as L_128, L_178, and SCB_L_128_10x5 to avoid large topological effects imposed by interchain entanglements. Figure 3.3.4 presents the results for the mean squared amplitude $<X_p^2>$ of the pth Rouse mode as a function of N/p^2 for each system. Note that only even modes (i.e., $p = 2, 4, 6, 8, \dots$) are allowed for ring polymers to satisfy the intrinsic closed-loop boundary conditions [13,14]. If a polymer behaves like an ideal Rouse chain, $<X_p^2>$ is given by

$$\left\langle X_p^2 \right\rangle = \frac{Nb^2}{2\pi^2 p^2} \qquad (3.3.3)$$

which indicates a linear plot of $<X_p^2>$ vs. N/p^2 (as represented by a dashed line of slope 1 in Fig. 3.3.4). Figure 3.3.4 shows that for all the simulated ring, linear, and SCB systems, Rouse prediction is fairly well satisfied for low p modes (i.e., $N/p^2 > 4$), but the deviation becomes larger for high p modes (i.e., $N/p^2 < 4$) due to the non-Gaussian structural characteristics for short subchains [14,34,35]. In more detail, $<X_p^2>$ at the lowest $p = 2$ mode for the ring systems corresponding to the overall chain dimensions of ring as $\left\langle X_2^2 \right\rangle = \left\langle R_d^2 \right\rangle / 2\pi^2 = 3\left\langle R_g^2 \right\rangle_{\text{ring}} / 2\pi^2$ appears to be slightly smaller than the Rouse prediction. This is attributed to the reduced overall chain dimension of rings (as being smaller than the Rouse prediction) via the nonconcatenation constraint [14,34] It is also important to notice that for a given normal mode p, $<X_p^2>$ for the SCB ring and linear polymers is slightly smaller than that for the bare ring and linear polymers with the same backbone length. Again, this is attributed to the relatively more compact chain structures of the SCB polymers due to the short branches.
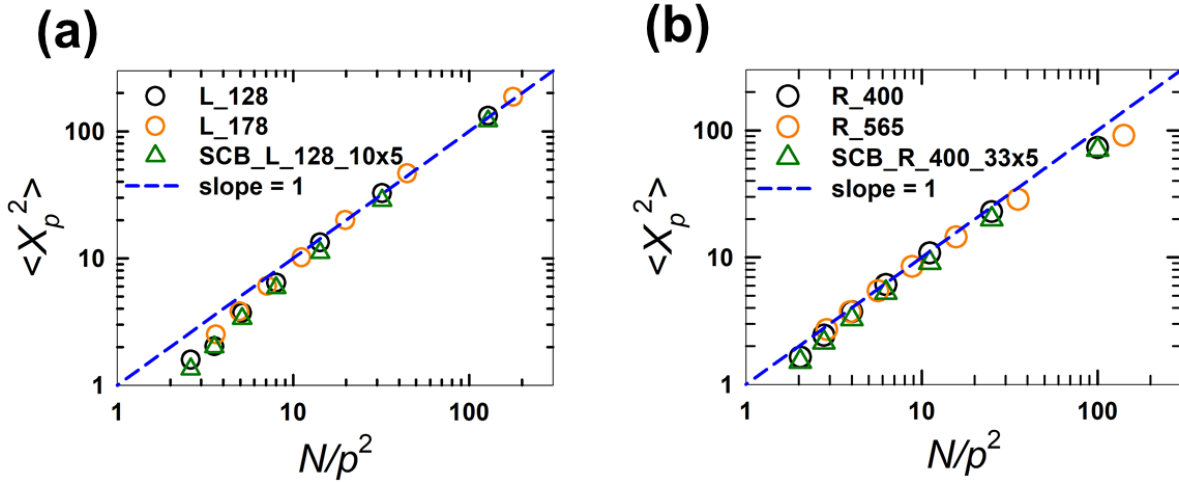
Figure 3.3.4. Mean squared amplitude of the Rouse normal modes $<X_p^2>$ as a function of N/p^2 (N being the number of backbone atoms) for (a) the bare and SCB linear PE, and (b) the bare and SCB ring PE melt systems. The blue dash line of slope 1 corresponds to the ideal Rouse behavior based on eqn (3.3.3).

We now look into the time autocorrelation function $\langle \mathbf{X}_p(t) \cdot \mathbf{X}_p(0) \rangle / \langle X_p^2 \rangle$ which is written for the Rouse model as [2,13,14]

$$\langle \mathbf{X}_p(t) \cdot \mathbf{X}_p(0) \rangle / \langle X_p^2 \rangle = \exp(-t/\tau_p) \qquad (3.3.4)$$

where the characteristic relaxation time τ_p for the pth normal mode is given by

$$\tau_p = \frac{\zeta N^2 b^2}{3\pi^2 k_B T} \frac{1}{p^2} \qquad (3.3.5)$$

where ζ denotes the monomeric friction coefficient and k_B Boltzmann's constant. Figure 3.3.5 presents a semi-log plot of $\langle \mathbf{X}_p(t) \cdot \mathbf{X}_p(0) \rangle / \langle X_p^2 \rangle$ vs. $p^2 t$ for the first seven normal modes for each polymer system. If the systems follow the Rouse scaling, the decay of the correlation functions for all normal modes would fall on a single straight curve. However, deviations from the ideal Rouse behavior appear for all the simulated ring, linear, and SCB PE systems. This is again ascribed to non-Gaussian characteristics via a higher degree of local structural stiffness for shorter subchains (comprising N/p monomers) corresponding to higher p modes [14,34,35]. Additionally, as consistent with the results for $<X_p^2>$, the decay of the correlation functions based on only the backbone atoms for the SCB ring and linear polymers is described quite well by the Rouse prediction compared to bare ring and linear systems. This feature seems to arise from the fact that the short branches, due to their very short characteristic time scales, relax in a time much shorter than the Rouse time scales of the backbone and play their dynamical role in constantly disturbing the backbone at the local branch points via their fast random motions, thus effectively promoting the Rouse dynamics of the backbone.
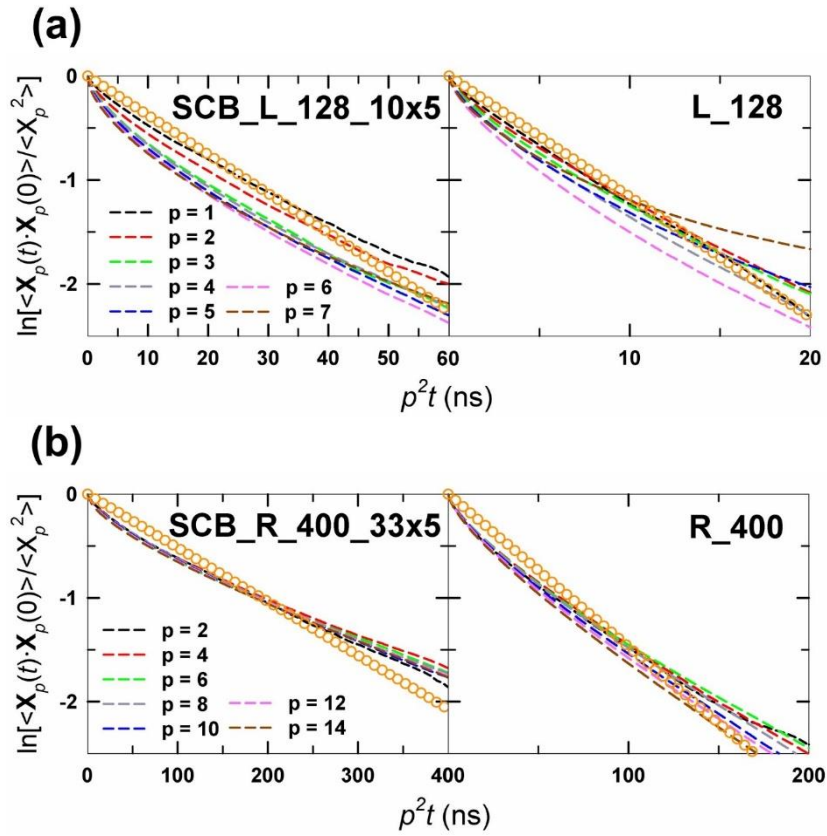
Figure 3.3.5. Normalized time autocorrelation functions of the first seven normal modes as a function of p^2t: (a) p = 1, 2, 3, 4, 5, 6, and 7 for the bare and SCB linear systems, and (b) p = 2, 4, 6, 8, 10, 12, and 14 for the bare and SCB ring systems. The orange symbols represent the ideal Rouse behavior based on eqns (3.3.4) and (3.3.5).

3.4. Conclusion

In this work, we carried out a detailed analysis on the influence of short branches on the structural and dynamical properties for the ring PE melts using atomistic MD simulations. To quantify the short-branching effects in conjunction with ring topology, the results of the SCB ring polymers were directly compared with those of the SCB linear polymers and bare polymers at the same backbone length. Our results clearly show that the SCB ring and linear polymers possess the overall compact molecular structures in association with the intrinsically compact branched architecture and the fast random movements of short branches constantly disturbing the overall chain. Furthermore, ring polymers, due to their intrinsic closed-loop geometry together with the nonconcatenation constraint between rings, generally exhibit significantly compact chain structures compared to the linear polymers. Similarly, the compact backbone structure of SCB polymers induced by the short branches reduces the degree of local structural non-Gaussian character for subchains in the short length scales, thus leading to a better consistency with the Rouse prediction compared to the bare polymers. Furthermore, the fast random movement of short branches due to their very short characteristic time scales constantly disturbs the chain backbone at the local branch points, effectively promoting the random Brownian (Rouse) dynamics of the backbone. In short, the structural compactness in conjunction with the fast dynamics of the short branches is supposed to result in the apparently more Rouse-like dynamics of the backbone of the SCB polymers. We also observed that the short branches make a significant influence on the local torsional characteristics along the chain backbone. In particular, the torsional modes directly involved with the branch points in the SCB ring and linear polymers exhibit distinctive populations of the *gauche-* and *trans*-states compared to the regular torsional mode in the corresponding bare polymers. Furthermore, the dynamics of the local torsional modes around the branch points appears to slow down considerably via an extra torsional stiffness imposed by the short branches.

Despite the lack of the current experimental technique to control precisely the branch distribution along the backbone as studied here, we expect rapid experimental advances in catalysts and chemical synthesis method to enable such control in the near future. It would be also interesting to examine the essential features found in this study in regard to the influences of short branches and ring topology on the structural and rheological behaviors of polymeric liquids under an external flow field.

3.5. References

(1) P.G. de Gennes, *J. Chem. Phys.* 1971, **55**, 572–579.

(2) M. Doi, S.F. Edwards, *The Theory of Polymer Dynamics*, first ed., Oxford University Press, New York, 1986.

(3) T.C.B. McLeish and R.G. Larson, *J. Rheol.* 1998, **42**, 81–110.

(4) T.C.B. McLeish, J. Allgaier, D.K. Bick, G. Bishko, P. Biswas, R. Blackwell, B. Blottière, N. Clarke, B. Gibbs, D.J. Groves, A. Hakiki, R.K. Heenan, J.M. Johnson, R. Kant, D.J. Read, and R.N. Yong, *Macromolecules* 1999, **32**, 6734–6758.

(5) M. Kapnistos, D. Vlassopoulos, J. Roovers, and L.G. Leal, *Macromolecules* 2005, **38**, 7852–7862.

(6) J.M. Kim and C. Baig, *J. Chem. Phys.* 2016. **144**, 081101.

(7) S.H. Jeong, J.M. Kim, and C. Baig, *Macromolecules* 2017, **50**, 4491–4500.

(8) S.H. Jeong, J.M. Kim, and C. Baig, *J. Rheol.* 2018, **62**, 1115–1124.

(9) S. Jeong, J.M. Kim, S. Cho, and C. Baig, *Soft Matter* 2017, **13**, 8644–8650.

(10) S. Brown, T. Lenczycki, and G. Szamel, *Phys. Rev. E* 2001, **63**, 052801.

(11) M. Kapnistos, M. Lang, D. Vlassopoulos, W. Pyckhout-Hintzen, D. Richter, D. Cho, T. Chang, and M. Rubinstein, *Nat. Mater.* 2008, **7**, 997–1002.

(12) Y. Doi, K. Matsubara, Y. Ohta, T. Nakano, D. Kawaguchi, Y. Takahashi, A. Takano, and Y. Matsushita, *Macromolecules* 2015, **48**, 3140–3147.

(13) H. Watanabe, T. Inoue, and Y. Matsumiya, *Macromolecules* 2006, **39**, 5419–5426.

(14) G. Tsolou, N. Stratikis, C. Baig, P.S. Stephanou, and V.G. Mavrantzas, *Macromolecules* 2010, **43**, 10692–10713.

(15) V. Arrighi, S. Gagliardi, A.C. Dagger, J.A. Semlyen, J.S. Higgins, and M.J. Shenton, *Macromolecules* 2004, **37**, 8057–8065.

(16) K. Hur, C. Jeong, R.G. Winkler, N. Lacevic, R.H. Gee, and D.Y. Yoon, *Macromolecules* 2011, **44**, 2311–2315.

(17) T. Vettorel, A.Y. Grosberg, K. Kremer, *Phys. Biol.* 2009, **6**, 025013.

(18) J. Suzuki, A. Takano, T. Deguchi, and Y. Matsushita, *J. Chem. Phys.* 2009, **131**, 144902.

(19) J.D. Halverson, W.B. Lee, G.S Grest, A.Y. Grosberg, and K. Kremer, *J. Chem. Phys.* 2011, **134**, 204904.

(20) A. Rosa and R. Everaers, *Phys. Rev. Lett.* 2014, **112**, 118302.

(21) J. Yoon, J. Kim, and C. Baig, *J. Rheol.* 2016, **60**, 673–685.

(22) K. Hur, R.G. Winkler, and D.Y. Yoon, *Macromolecules* 2006, **39**, 3975–3977.

(23) D. Michieletto, D. Marenduzzo, E. Orlandini, and M.S. Turner, *Polymers* 2017, **9**, 349.

(24) Z. Yan, S. Costanzo, Y. Jeong, T. Chang, and D. Vlassopoulos, *Macromolecules* 2016, **49**, 1444–

1453.

(25) E. Lee, S. Kim, and Y. Jung, *Macromol. Rapid Commun.* 2015, **36**, 1115–1121.

(26) D.G. Tsalikis, V.G. Mavrantzas, and D. Vlassopoulos, *ACS Macro Lett.* 2016, **5**, 755–760.

(27) S. Jeong, S. Cho, J.M. Kim, and C. Baig, *Macromolecules* 2018, **51**, 4670–4677.

(28) S. Nosé, *Mol. Phys.* 1984, **52**, 255-268.

(29) W.G. Hoover, *Phys. Rev. A* 1985, **31**, 1695-1697.

(30) M. Tuckerman, B.J. Berne, and G.J. Martyna, *J. Chem. Phys.* 1992, **97**, 1990-2001.

(31) M.G. Martin and J.I. Siepmann, *J. Phys. Chem. B* 1999, **103**, 4508-4517.

(32) B.H. Zimm and W.H. Stockmayer, *J. Chem. Phys.* 1949, **17**, 1301-1314.

(33) P.J. Flory, *Statistical Mechanics of Chain Molecules*, first ed., John Wiley & Sons, New York, 1969.

(34) D.G. Tsalikis, T. Koukoulas, V.G. Mavrantzas, R. Pasquino, D. Vlassopoulos, W. Pyckhout-Hintzen, A. Wischnewski, M. Monkenbusch, and D. Richter, *Macromolecules* 2017, **50**, 2565-2584.

(35) V.A. Harmandaris, V.G. Mavrantzas, and D.N. Theodorou, *Macromolecules* 1998, **31**, 7934-7943.

Chapter 4. Nonequilibrium Monte Carlo simulations of entangled polymer melts under steady shear flow

4.1. Introduction

Due to their enormous intramolecular degree of freedom, polymers generally exhibit a variety of complex structural and rheological behaviors (e.g., shear thinning and thickening,[1,2] strain hardening,[3-5] melt fracture,[6,7] flow-induced crystallization,[8-10] and phase separation[11]) under external flow fields. To properly analyze the rheological properties for concentrated polymer solutions or melts, we need to account for the effect of spatial and dynamical intermolecular correlations caused by the mutual interactions between different polymer chains. Although the computer simulations have been proven very beneficial for understanding the complicated macroscopic rheological behaviors of polymer systems at fundamental molecular level [12-19], it has been applied to short-chain polymers rather than those employed in practical applications due to the time-cost problem.[20,21] To overcome this, a nonequilibrium Monte Carlo (MC) methodology was developed based on the GENERIC (General Equation for the NonEquilibrium Reversible-Irreversible Coupling) thermodynamic formalism [22,24] for simulating polymer melts undergoing external flow with reasonable computational costs. [25-30] The methodology incorporates an additional field energy term into the expanded statistical ensemble. Guided by the well-established polymer kinetic theory, [31] a second-rank conformation tensor based on the chain end-to-end vector was adopted as the nonequilibrium structural variable and the corresponding conjugate thermodynamic force variable was introduced to account for the flow field. The study showed that overall the GENERIC MC method appears capable of qualitatively (and even quantitatively up to a certain intermediate flow strength) reproducing the deformed structures of polymer systems under shear and elongational flows as obtained from NEMD simulations. [28-30]

With such promising features of the GENERIC MC methodology, in this study we have further extended it to simulate entangled polymer melts under steady shear flow. To this end, similar to unentangled polymers, we have adopted the conformation tensor as a proper structural variable that represents the overall nonequilibrium structures of entangled polymeric systems. In view of a potential use of GENERIC MC in conjunction with NEMD for simulating long polymer systems in practical applications, here we have made a detailed analysis on the predictive capabilities of the GENERIC MC for a variety of structural and rheological properties in a wide range of flow strengths with direct comparison between the MC and NEMD results.

4.2. Simulation methods and Materials studied

In this study, we carried out GENERIC MC and NEMD simulations of the $C_{400}H_{802}$ entangled linear polyethylene (PE) melt under shear flow at constant temperature $T = 450$ K and density $\rho = 0.7640$ g/cm^3 (corresponding to the pressure $P = 1$ atm).[32] The nonequilibrium states spanning from linear to highly nonlinear viscoelastic regimes were selected, corresponding to the Deborah numbers ($\text{De} \equiv \lambda\dot{\gamma}$) in the interval of $0.5 \leq \text{De} \leq 540$ based on the imposed shear rate $\dot{\gamma}$ and the longest relaxation time $\lambda = 218 \pm 10$ ns of the system. A sufficiently large number (i.e., 198) of molecules were used in the simulations with the box dimensions being set to (318.8 Å × 86.96 Å × 89.96 Å) along the x-, y-, and z-directions, respectively, as enlarged in the flow (x-) direction to avoid undesirable system-size effects due to the significant chain stretch and alignment at high shear rates. The chain radius of gyration R_g at equilibrium was calculated as equal to 36.6 Å for the C_{400} PE system. Thus, the box dimensions in the velocity gradient (y-) and neutral (z-) directions were set to more than twice as large as R_g.

Briefly describing the general features of the GENERIC MC methodology, the extended expression of the internal energy function U for entangled polymeric systems under external flow fields is written as

$$U = TS - PV + \mu N_{ch} + N_{seg} k_B T \boldsymbol{\alpha} : \tilde{\mathbf{c}}_{seg}, \qquad (4.2.1)$$

implying that

$$dU = TdS - PdV - \mu dN_{ch} + k_B T \boldsymbol{\alpha} : d\left(N_{seg}\tilde{\mathbf{c}}_{seg}\right) \qquad (4.2.2)$$

where N_{seg} denotes the total number of entanglement segments, $\tilde{\mathbf{c}}_{seg} = 3\langle \mathbf{R}_{seg}\mathbf{R}_{seg}\rangle / \langle R_{seg}^2\rangle_{eq}$ the conformation tensor based on the entanglement segment vector $\mathbf{R}_{seg}$, and the subscript eq the equilibrium condition, and $\boldsymbol{\alpha}$ the conjugate thermodynamic field corresponding to $\tilde{\mathbf{c}}_{seg}$ accounting for the flow effects, S the entropy, μ the chemical potential, and k_B Boltzmann's constant. Other thermodynamic functions such as the generalized Helmholtz free energy A and Gibbs free energy G can also be derived through appropriate Legendre transforms: [28,29,33]

$$dA\left(T,V,N_{ch},N_{seg}\tilde{\mathbf{c}}_{seg}\right) = -SdT - PdV + \mu dN_{ch} + k_B T\boldsymbol{\alpha} : d\left(N_{seg}\tilde{\mathbf{c}}_{seg}\right), \qquad (4.2.3)$$

$$dA'\left(T,V,N_{ch},\boldsymbol{\alpha}\right) = -SdT - PdV + \mu dN_{ch} - N_{seg}\tilde{\mathbf{c}}_{seg} : d\left(k_B T\boldsymbol{\alpha}\right) \qquad (4.2.4)$$

and

$$dG\left(T,P,N_{ch},\boldsymbol{\alpha}\right)=-SdT+VdP+\mu dN_{ch}-N_{seg}\tilde{\mathbf{c}}_{seg}:d\left(k_{B}T\boldsymbol{\alpha}\right). \tag{4.2.5}$$

The GENERIC MC simulations are executed based on eqn (4.2.4) in an expanded ensemble ($N_{ch}NVT\boldsymbol{\mu}^{*}\boldsymbol{\alpha}$) [25-30,33] where the following variables are specified: the number of polymer chains N_{ch}, the average number of atoms per chain N, the volume V, the temperature T, the spectrum of chain relative chemical potentials $\boldsymbol{\mu}^{*}$ controlling the distribution of chain lengths, and the thermodynamic field $\boldsymbol{\alpha}$. The corresponding probability distribution function in the expanded ensemble is given as

$$\rho^{N_{ch}NVT\boldsymbol{\mu}^{*}\boldsymbol{\alpha}}\left(\mathbf{r}_{1},\mathbf{r}_{2},\cdots,\mathbf{r}_{n},V\right)\sim\exp\left[-\beta\left\{U\left(\mathbf{r}_{1},\mathbf{r}_{2},\cdots,\mathbf{r}_{n},V\right)-\sum_{k=1}^{N_{ch}}\mu_{k}^{*}N_{k}-k_{B}T\boldsymbol{\alpha}:\sum_{i=1}^{N_{seg}}\tilde{\mathbf{c}}_{seg,i}\right\}\right] \tag{4.2.6}$$

which implies that the nonequilibrium configurational space of the system can be explored according to the following modified Metropolis criterion:

$$P_{acc}^{N_{ch}NVT\boldsymbol{\mu}^{*}\boldsymbol{\alpha}}\sim\exp\left[-\beta\left\{\Delta U-\sum_{k=1}^{N_{ch}}\Delta\left(\mu_{k}^{*}N_{k}\right)-k_{B}T\boldsymbol{\alpha}:\sum_{i=1}^{N_{seg}}\Delta\tilde{\mathbf{c}}_{seg,i}\right\}\right] \tag{4.2.7}$$

Here, $\beta\equiv 1/k_{B}T$, n $\left(n=\sum_{k=1}^{N_{ch}}N_{k}\right)$ is the total number of atoms in the system, μ_{k}^{*} the relative chemical potential of the kth chain consisting of N_{k} atoms, $\tilde{\mathbf{c}}_{seg,i}$ the conformation tensor of the ith segment. Based on experimental data, [34] *i.e.*, the entanglement molecular weight $M_{e}=920$ g/mol for HDPE (high density polyethylene) at $T=443$ K and $\rho=0.768$ g/cm^{3}, the average number N_{e} of carbon atoms per entanglement segment for the C$_{400}$ PE melt system in this study is estimated as $N_{e}\approx 68$. Accordingly, in GENERIC MC simulations we applied the thermodynamic field $\boldsymbol{\alpha}$ to each individual entanglement segment (consisting of approximately 68 carbon atoms) starting from the chain ends. We note that the application of the field to the entanglement segment vector for entangled PE melts essentially corresponds to that based on the chain end-to-end vector for unentangled PE melts. This feature is consistently reflected in theoretical descriptions of the structural and rheological behaviors with respect to the entanglement segment vector for long entangled melts and to the chain end-to-end vector for short unentangled melts. [10,14,17,18,31,34,36] It is thus considered the comparison for the $\boldsymbol{\alpha}$ tensor between the entangled and unentangled PE systems to be meaningful from both physical and numerical viewpoints. We also mention that with the expression of $\boldsymbol{\alpha}=\dfrac{1}{k_{B}T}\dfrac{\partial A}{\partial\left(N_{seg}\tilde{\mathbf{c}}_{seg}\right)}$ (where the linear part for the temperature effect is separated based on the classical rubber theory) from eqn (4.2.3), the thermodynamic force field $\boldsymbol{\alpha}$ is dimensionless. As the field tensor plays a role of the external flow field driving the polymer systems to certain nonequilibrium states, it is closely related to the applied

shear force or shear rate, i.e., more directly to the dimensionless shear rate (i.e., $De \equiv \lambda\dot{\gamma}$). With the chosen structure variable $\tilde{\mathbf{c}}_{seg}$, the (elastic) stress tensor can be derived as: [28,29]

$$\tau_{\alpha\beta} = \frac{2}{V}\tilde{c}_{seg,\alpha\gamma}\frac{\delta A(\tilde{\mathbf{c}}_{seg})}{\delta\tilde{c}_{seg,\gamma\beta}} = \frac{2k_B T}{V}N_{seg}\tilde{c}_{seg,\alpha\gamma}\alpha_{\gamma\beta} \tag{4.2.8}$$

As effectively applied to simulate unentangled polymer melts in previous studies, [28,29] the following simplified form of $\boldsymbol{\alpha}$ with setting $\alpha_{zz} = 0$ (based on most viscoelastic models) was adopted in the present GENERIC MC simulations for entangled melts:

$$\boldsymbol{\alpha} = \begin{pmatrix} \alpha_{xx} & \alpha_{xy} & 0 \\ \alpha_{xy} & \alpha_{yy} & 0 \\ 0 & 0 & 0 \end{pmatrix}, \tag{4.2.9}$$

The initial values for the three nonzero components (α_{xx}, α_{xy}, and α_{yy}) in GENERIC MC simulations were estimated based on the results of $\boldsymbol{\alpha}$ for each De number obtained for the corresponding unentangled PE melts. [28,29] Although the initial values were a good starting point, they turned out to be insufficiently accurate for quantitative comparison. Therefore, an iteration process was carried out to achieve convergence between the GENERIC MC and NEMD data for $\tilde{\mathbf{c}}_{ete} = 3\langle\mathbf{R}_{ete}\mathbf{R}_{ete}\rangle / \langle R_{ete}^2\rangle_{eq}$ based on the longest-scale chain end-to-end vector $\mathbf{R}_{ete}$, because the dynamical and rheological properties of polymer melt systems are mostly determined by the largest-scale chain structures. [31,36]

For GENERIC MC simulations, a small polydispersity $I \approx 1.083$ was introduced with a uniform chain length distribution in the range of $C_{200}H_{402}$ to $C_{600}H_{1202}$ in conjunction with an efficient chain-connectivity altering end-bridging move. [37] In the MC simulations, the following mix of MC moves were used; end-bridging, 50%; concerted rotation, 32%; reptation, 10%; flip, 6%; and end-mer rotation, 2%. [25,37,38]

NEMD simulations were executed with the *p*-SLLOD algorithm, [39] implemented by a Nosé-Hoover thermostat [40,41] and the standard Lees–Edwards sliding brick boundary conditions. [42] The set of evolution equations in the NEMD method was numerically integrated using an efficient *r*-RESPA (reversible reference system propagator algorithm) [43] with two different time scales in an MD step; 0.47 fs for the fast bonded (bond-stretching, bond-bending, and bond-torsional) interactions and 2.35 fs for the slow non-bonded intermolecular and intramolecular Lennard-Jones (LJ) interactions, the thermostat, and the flow field. The well-known Siepmann-Karaborni-Smit (SKS) united-atom potential model [44] was adopted for both GENERIC MC and NEMD simulations, except for that the rigid bond in the original model was replaced by a harmonic flexible one for the NEMD.

4.3. Results and Discussion

Figure 4.3.1 presents the result of thermodynamic force field field α for the simulated $C_{400}H_{802}$ entangled PE system as a function of De number, compared to those of the unentangled systems ($C_{50}H_{102}$, $C_{78}H_{158}$, and $C_{128}H_{258}$) [28,29] (note that the field tensor α conjugates to $\tilde{\mathbf{c}}_{ete}$ for unentangled PE systems and $\tilde{\mathbf{c}}_{seg}$ for entangled PE systems).
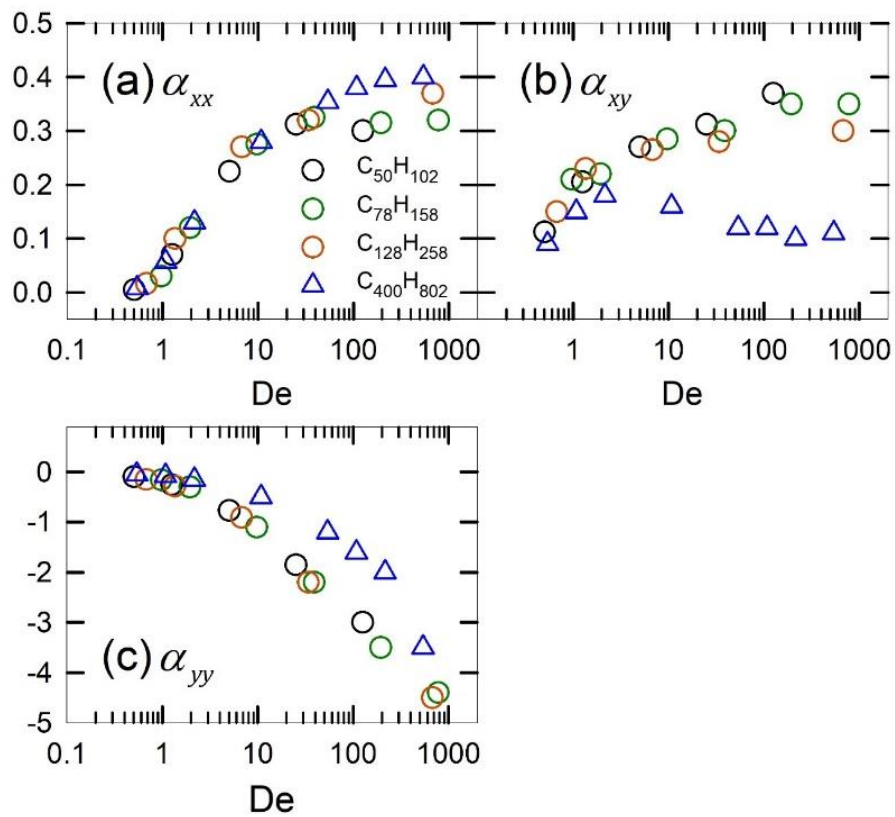
Figure 4.3.1. Comparison of the (a) *xx*, (b) *xy*, and (c) *yy* components of the thermodynamic force field α between the entangled $C_{400}H_{802}$ and unentangled ($C_{50}H_{102}$, $C_{78}H_{158}$, $C_{128}H_{258}$) [28,29] polyethylene melts as a function of De number. The error bars are smaller than the size of the symbols.

First, both the entangled and unentangled systems exhibit increases of the α_{xx} and α_{xy} values but a dec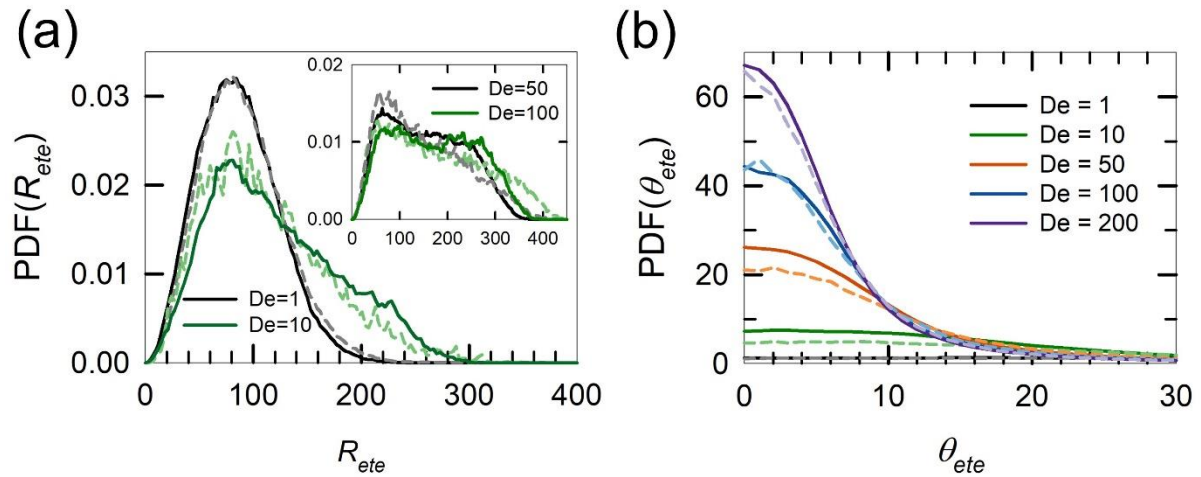rease of the α_{yy} value, as the shear rate increases at low flow strengths. This trend reflects the fact that chains become more and more aligned and stretched to the flow direction with increasing the applied shear. Furthermore, α_{xy} appears to be larger than α_{xx} in magnitude in this flow regime where chains are likely to be oriented in the flow direction without significant structural distortions.[12-14,19] In the intermediate flow regime, α_{xx} is shown to increase rapidly with increasing De number for all systems, indicative of considerable deformation of the overall chain structure. In high flow fields, each system approaches a plateau value for α_{xx}, because the average chain extension becomes saturated in conjunction with intensive chain rotation and tumbling behaviors under shear in the strong flow regime. The specific De numbers where the overall chain dimension is nearly constant generally depend on the chain length; e.g., further chain stretch can occur in the entangled C_{400} PE system beyond the range of De numbers depicted in Fig. 1a. [14] For α_{xy}, while the unentangled systems exhibit a gradual increase with increasing De number in the intermediate flow regime and saturation at high flow strengths, the entangled C_{400} PE melt shows decreasing behavior in the intermediate flow regime. This can be attributed to the stronger chain alignment and xy-correlations of the long entangled polymers for a given flow field compared to the relatively short unentangled polymers, beyond the weak flow strengths. [12,14,19] In contrast to α_{xx} and α_{xy}, α_{yy} decreases rather quickly with increasing De number in the intermediate-to-strong flow regimes for both entangled and unentangled PE systems, accounting for a large decrease in the overall chain dimension for the velocity gradient (y-) direction due to chain alignment and stretch along the flow (x-) direction. Quantitatively, the magnitude of α_{yy} appears somewhat smaller for the C_{400} PE melt than the unentangled systems. Considering the intrinsic methodological feature of GENERIC MC for applying a uniform thermodynamic force field to each entanglement segment independently, the general characteristics of the thermodynamic field tensor shown by the C_{400} PE melt systems can be good guideline to carry out the GENERIC MC simulations for other entangled polymer systems.
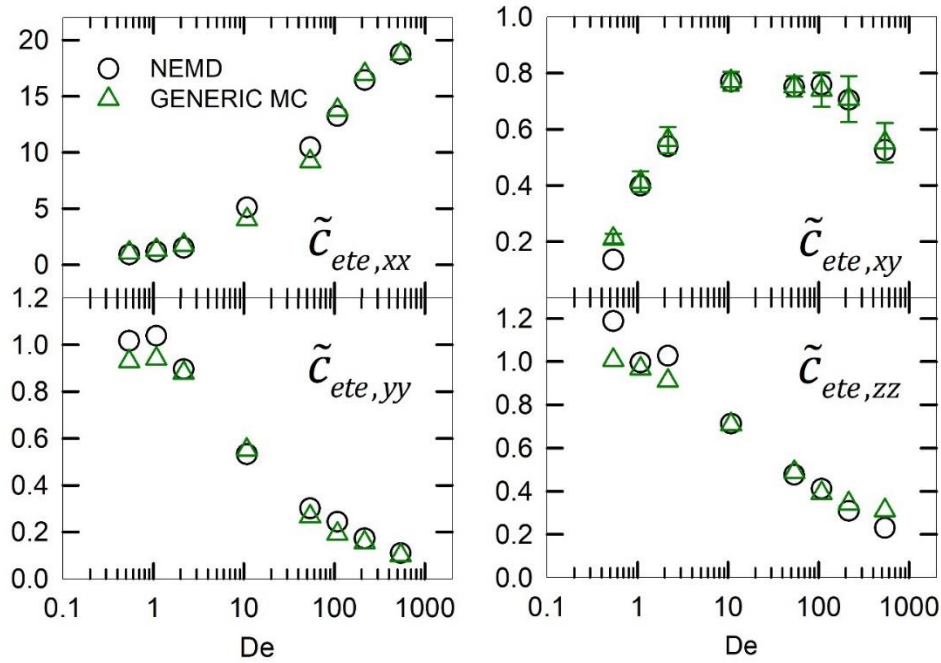
Figure 4.3.2. Comparison between GENERIC MC and NEMD for the *xx*, *xy*, *yy*, and *zz* components of the conformation tensor $\tilde{\mathbf{c}}_{ete}$ as a function of De number for the simulated $C_{400}H_{802}$ entangled PE melt. The error bars are smaller than the size of the symbols unless specified otherwise.

In Fig. 4.3.2, we compare the four components of the conformation tensor $\tilde{\mathbf{c}}_{ete}$ based on the chain end-to-end vector between GENERIC MC and NEMD simulations for the C_{400} entangled PE system at various De numbers. Overall, the two methods show excellent agreement with each other for *xx*, *xy*, and *yy* components at all shear rates. While this result apparently indicates that the present iteration procedure numerically works, in view of generally very complex rheological influences by the flow exhibited by real polymer systems (in conjunction with an enormous number of configurational degrees of freedom at atomistic level), it further shows that the simple GENERIC MC approach adopted in this study can properly represent the large-scale nonequilibrium structures for entangled polymer systems. Based on these results, the information of the α tensor obtained by GENERIC MC in conjunction with NEMD can be used to evaluate the fundamental nonequilibrium thermodynamic functions (energy, entropy, and Helmholtz free energy) of flowing polymeric systems through thermodynamic integration [i.e., eqns (4.2.1), (4.2.2), and (4.2.4)]. Interestingly, despite our choice of $\alpha_{zz} = 0$, the result of $\tilde{c}_{ete,zz}$ for GENERIC MC appears to quantitatively match that of NEMD. However, this agreement is considered rather fortuitous, as a large overall discrepancy of $\tilde{c}_{ete,zz}$ was observed between the two methods for unentangled melt systems in previous studies.[28,29]

Figure 4.3.3. (a) Comparison of the probability distribution function (PDF) of the chain end-to-end distance $|\mathbf{R}_{ete}|$ between GENERIC MC (dashed lines) and NEMD (solid lines) for the simulated $C_{400}H_{802}$ entangled PE melt at various De numbers. For clarity, the results at high De numbers are presented separately in the inset. To alleviate the influence of polydispersity for the GENERIC MC simulations, only chains whose length is in the range $C_{350}H_{702}$–$C_{450}H_{902}$ were included in the calculation.(b) Comparison between GENERIC MC (dashed lines) and NEMD (solid lines) for the probability distribution of the orientation angle of the chain end-to-end vector (θ_{ete}) with respect to the flow direction as a function of De number.

Figure 4.3.3(a) shows a more detailed structural comparison between the GENERIC MC and NEMD simulations for the probability distribution of the chain end-to-end distance $|\mathbf{R}_{ete}|$ at various De numbers. For low-to-intermediate flow strengths (up to De numbers approximately equal to 10), the GENERIC MC method quite successfully reproduces the overall skewed non-Gaussian distribution of the chain size as obtained by the NEMD. For larger flow strengths, the NEMD simulations show that the distribution becomes rather flattened in the intermediate regime of $|\mathbf{R}_{ete}|$ with two characteristic peaks at small and large values of $|\mathbf{R}_{ete}|$ in association with the chain rotation and stretching behaviors, respectively. [14,19,45] While the GENERIC MC method still provides overall consistency with NEMD even for rather high flow fields (De > 50), it does not correctly predict the two pronounced peaks and the flattened region in between; rather, it produces a smoothly declining and broadened distribution for larger values of $|\mathbf{R}_{ete}|$. This is attributed to the nature of the GENERIC MC thermodynamic force field that is applied to all entanglement segments along the chain uniformly and independent of each other. Such a field cannot adequately account for the complex structural and dynamical correlations between the segments under flow. It is further noted that the GENERIC MC method, by its intrinsic static nature, cannot capture the chain rotational and tumbling dynamics that occur in real polymeric materials undergoing shear flow as observed in NEMD simulations. Despite these features, the GENERIC MC method can quite faithfully describe the general trends of chain deformation and orientation under shear for a wide range of flow strengths.

Figure 4.3.3(b) compares GENERIC MC and NEMD for the probability distribution of the orientation angle θ_{ete} based on the chain end-to-end vector. As the flow strength increases, polymer chains become more aligned to the flow direction, resulting in the increase of the population at the angular region of $0° \leq \theta_{ete} \leq 20°$. Although quantitative differences appear between the two methods for intermediate-high flow regime, the overall distribution is quantitatively quite consistent with each other, implying the capabilities of the GENERIC MC for reproducing the global chain orientation with respect to the applied flow.

Further structural information can be obtained via the Brightness method that characterizes various atomistic chain configurations into several representative mesoscopic structures. [46,47] The mesoscale configuration for each chain was determined based on the bead distribution along the chain without regard to the actual chain size. Figure 4.3.5 compares GENERIC MC and NEMD for the probability distribution of the mesoscale chain configurations with respect to the applied flow strength. At very weak flow strengths (i.e., De ≤ 2), the PDFs are not much disturbed by the external flow. At intermediate flow strengths (i.e., $10 \le De \le 54$), the polymer chains are significantly deformed by overall chain stretching and alignment in the flow direction, leading a sharp rise in the Half-dumbbell and Stretched configurational portions and diminish in the Kink and Coil portions. [47,48]
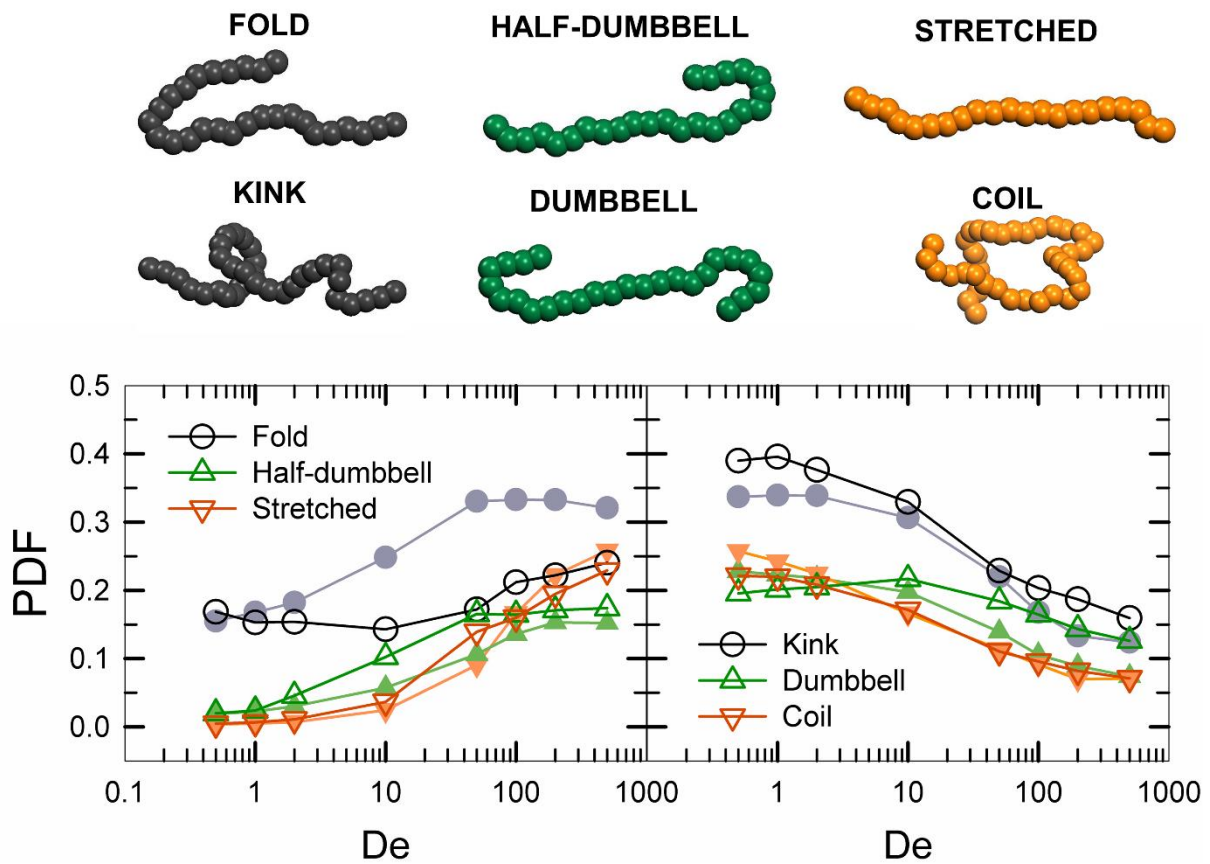
Figure 4.3.5. Comparison between GENERIC MC (filled symbols) and NEMD (open symbols) for the distribution of the six representative mesoscale chain configurations (Fold, Half-dumbbell, Stretched, Kink, Dumbbell, and Coil) obtained by the Brightness method at various De numbers. A simple conformation sketch for the six mesoscale chain structures is presented above the plot.

At strong flow regime (De ≥ 108), in addition to the continuous increase in the stretched configurations such as Half-dumbbell and Stretched, the Fold portion gradually increases in proportion with the increasing shear rate via hairpin-like chain rotation and tumbling dynamics under shear. [47-49] Overall, the GENERIC MC method accurately predicts the NEMD results of the increasing trend of the three configurations (Fold, Half-dumbbell, and Stretched) and decreasing trend of the other three configurations (Kink, Dumbbell, and Coil). Specifically, quantitative consistencies between the two methods are obtained for low-to-intermediate flow strengths (up to De ≈ 10). As the flow strength increases further, however, significant inconsistencies appear between the two methods for each configuration. It is mainly attributed to the intrinsic inability of the GENERIC MC method to accommodate any dynamic information. In this regard, it is interesting that the GENERIC MC method gives rise to a dramatic increase of the Fold configuration in the intermediate flow regime. This result is considered due to the mean-field nature of thermodynamic force field which is uniformly and independently applied to individual entanglement segment in the GENERIC MC method. Increasing the field strength brings out the enhancement in the degree of the average segmental orientation and stretch without accounting for any dynamical correlations between different segments along the chain; e.g., chain tumbling occurs via the differences in the streaming velocity between different segments depending on their relative positions in the velocity gradient direction of the shear flow. [49] Therefore, as the flow strength increases, the GENERIC MC method tends to decrease the mesoscopic chain configurations (such as Dumbbell and Kink) that require locally crowded inhomogeneous bead distributions along the chain, and instead increase the configurations (such as Stretched and Fold) characterized with rather uniform bead distributions.

We now turn our attention to the topological properties of the entangled linear C_{400} PE melts. The entanglement network of the system was attained by applying a Z1-algorithm. [50,51]
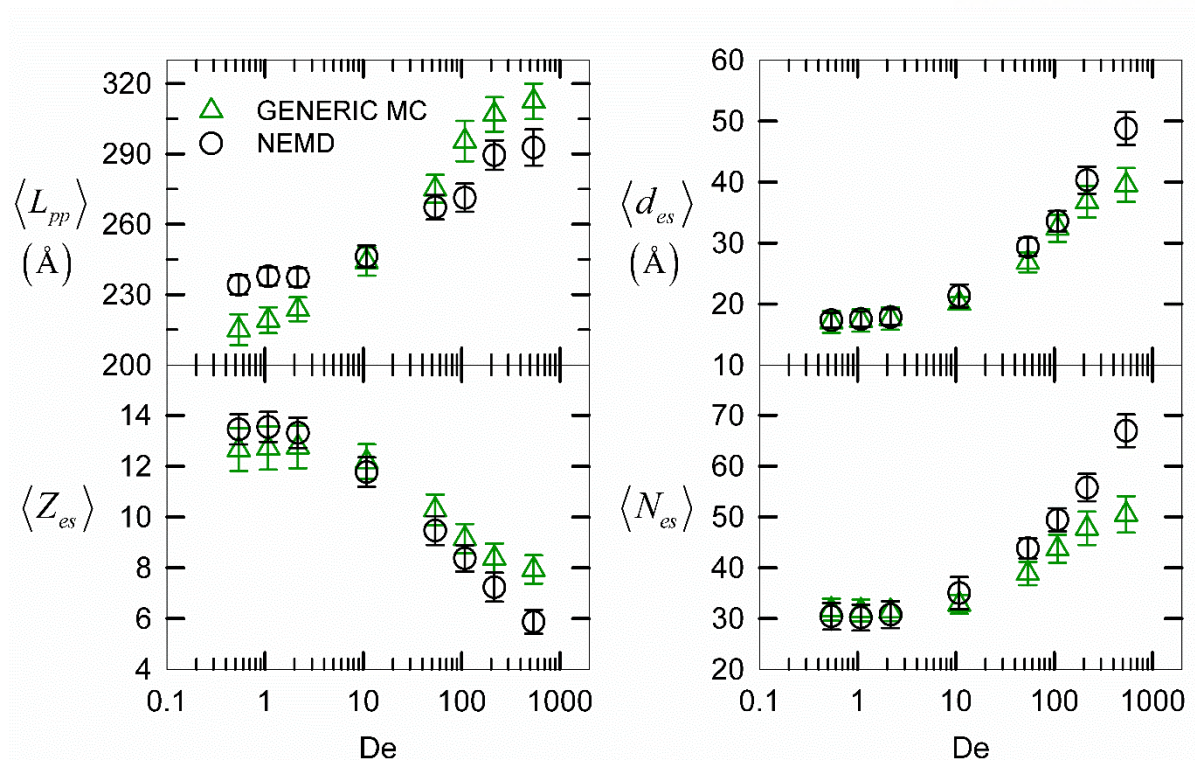
Figure 4.3.6 Comparison between GENERIC MC and NEMD for the representative topological measures obtained by the Z1-code [50,51] at various De numbers; the average primitive path (PP) contour length $\langle L_{pp} \rangle$, the average number of entanglement strands $\langle Z_{es} \rangle$ per chain, the average end-to-end length $\langle d_{es} \rangle$ of an entanglement strand, and the average number of carbon atoms $\langle N_{es} \rangle$ per entanglement strand. The GENERIC MC results involve selective chain lengths in the range of $C_{380}H_{762}$ to $C_{420}H_{842}$ to relieve the influence of polydispersity.

Figure 4.3.6 presents the results for the four representative topological measures, the average primitive path (PP) contour length $\langle L_{pp} \rangle$, the average number of entanglement strands $\langle Z_{es} \rangle$ per chain, the average end-to-end length $\langle d_{es} \rangle$ of an entanglement strand, and the average number of carbon atoms $\langle N_{es} \rangle$ per entanglement strand. In weak flow fields (De ≤ 2), the topological properties appear practically unaffected by the flow as shown by the GENERIC MC and NEMD simulations. As the flow strength further increases, significant changes occur in the network properties due to the large chain extension and alignment. We note that chain stretch tends to increase all topological properties, whereas chain alignment decreases the degree of topological interactions between chains, thus reducing $\langle Z_{es} \rangle$ and $\langle L_{pp} \rangle$. [14] It is seen that the GENERIC MC method produces a relatively larger increase of $\langle L_{pp} \rangle$ while increasing flow strength in the intermediate flow regime compared to the NEMD, indicating a higher degree of average chain extension for a given flow field. As stated above, this is ascribed to the uniform force field in the entanglement level adopted in the GENERIC MC method, which is consistent with the results of Figure 4.3.3a. This trend of $\langle L_{pp} \rangle$ appears consistently reflected in the result of $\langle Z_{es} \rangle$ for which the GENERIC MC predicts a lesser degree of decrease as the De number increases compared to the NEMD (this is also consistent with the relatively lesser degree of overall chain alignment by the GENERIC MC simulations shown in Figure 4.3.3b). However, $\langle d_{es} \rangle$ and $\langle N_{es} \rangle$ appear somewhat smaller for GENERIC MC, particularly at high De numbers. This result is partly correlated with that of $\langle Z_{es} \rangle$. We note that small deviations at low De numbers between GENERIC MC and NEMD are ascribed to the polydispersity effect of surrounding chains that impose interchain entanglements on the (approximately) C_{400} chains. Overall, the GENERIC MC method is considered to reproduce the general trends of the variations in the entanglement network with respect to the applied shear flow fairly well.
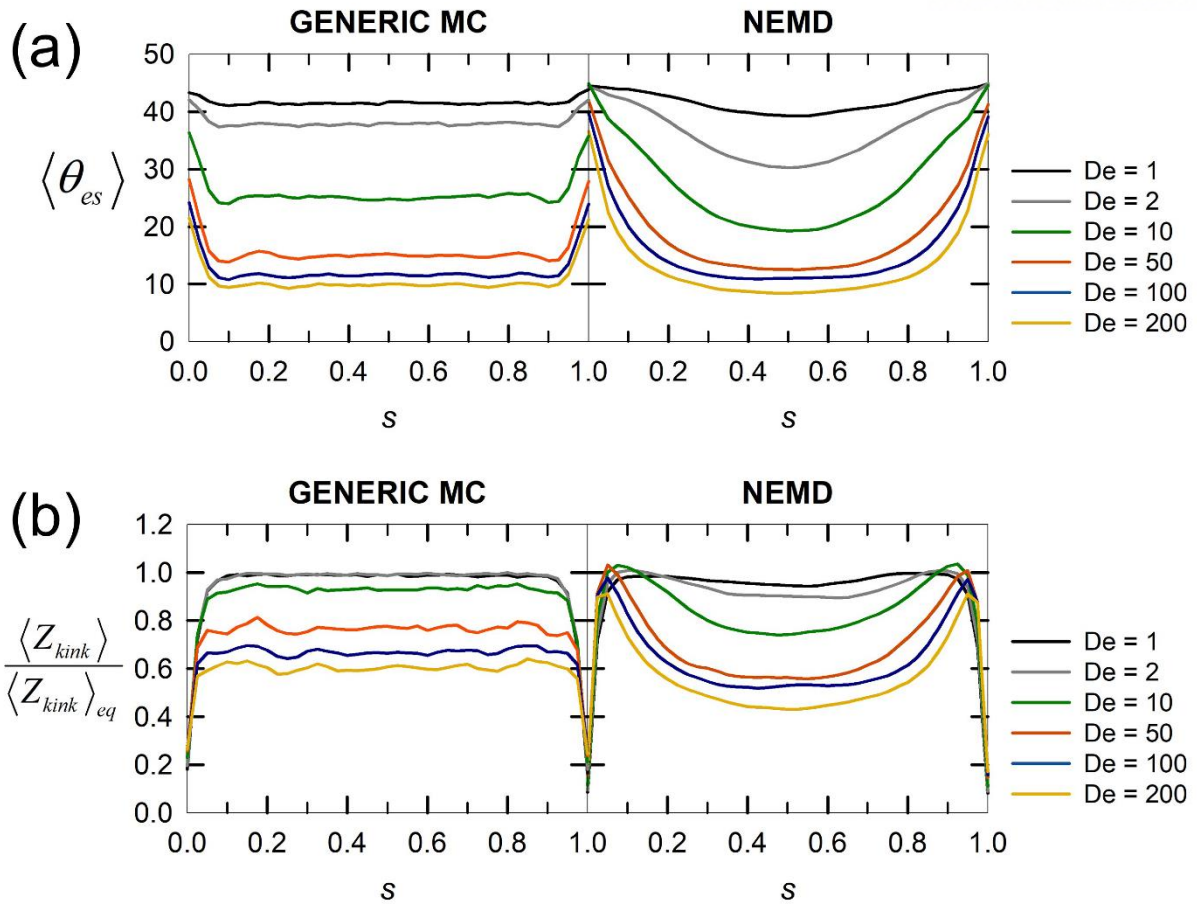
Figure 4.3.7. Comparison between GENERIC MC and NEMD for (a) the average orientation angle based on entanglement segment vector $\langle \theta_{es} \rangle$ and (b) the average number of entanglement (kink) points $\langle Z_{kink} \rangle$ (normalized by the equilibrium value) with respect to the (normalized) PP contour segment s ranging from 0 to 1. For adequate comparison, only the chains whose length is in the range $C_{380}H_{762}-C_{420}H_{842}$ were involved in the GENERIC MC results.

Figure 4.3.7 shows a more detailed comparison of the entanglement network between GENERIC MC and NEMD. In Fig. 7a, we analyzed the average orientation angle of the entanglement strands with respect to their position along the chain, i.e., the normalized PP contour segment *s* ranging from 0 to 1. At very weak flow strength (De $\approx$ 1), both simulation methods show $\langle \theta_{es} \rangle \approx 45°$ consistently along the whole contour PP. As the shear rate increases, the NEMD simulations exhibit an overall non-uniform alignment of the entanglement segments strongly dependent on their locations relative to the chain ends, i.e., a lesser degree of alignment to the applied flow direction as the segment becomes closer to a chain end (*s* = 0 or 1). This result is physically reasonable considering that the chain ends possess relatively high thermal mobility due to the large free volume around them. In comparison, GENERIC MC shows a nearly uniform alignment of chain segments along the whole chain except for those segments very close to the chain ends. As mentioned above, this is attributed to the uniformly and independently applied thermodynamic force field for the individual chain segments, irrespective of their location along the chain, in the GENERIC MC method.

Furthermore, in Fig. 4.3.7(b), we analyze the probability distribution for the average number of entanglement points (kinks) per chain as a function of the segmental position along the chain. Consistent with the monotonic decrease of $\langle Z_{es} \rangle$ with the increasing shear rate (Fig. 6), the whole curve of $\langle Z_{kink} \rangle$ is seen to move downward as the De number increases for both GENERIC MC and NEMD simulations. However, the overall shape of the plot differs noticeably between the two methods. Similar to the result for $\langle \theta_{es} \rangle$ in Fig. 4.3.7(a), the GENERIC MC gives rise to an overall uniform distribution throughout the chain (except for those segments very close to the chain ends), which is in sharp contrast with the NEMD results that show a non-uniform distribution with a strong dependence of $\langle Z_{kink} \rangle$ on the segmental position. The NEMD reveals that as the De number increases, the relative value of $\langle Z_{kink} \rangle$ increases when the segmental position is closer to the chain end and concomitantly decreases toward the chain center. This result is directly associated with the increase in the degree of the overall chain alignment to the flow direction as the flow strength increases such that the entanglements formed between two neighboring chains tend to move toward the chain ends as they become more aligned to each other. However, such interchain correlative behaviors are mostly missing in the GENERIC MC method due to its intrinsic mean-field approach such that the nonequilibrium thermodynamic field is (i) uniformly applied to all chain segments irrespective of their positions along the chain and (ii) independently applied to the individual chains without regard to any spatial and dynamical correlations between the chains.

4.4. Conclusion

In this study, we further extended the application of nonequilibrium GENERIC MC methodology with a proper choice of structural variable to simulate entangled polymeric melt systems under an external shear flow. In order to address the basic aspects on the performance of the GENERIC MC method, we directly compared the MC results with those obtained from NEMD method which has been widely applied to simulate realistic polymer systems under various flow conditions in favorable comparison with available experimental data and polymer models. Direct comparison between two methods for various structural, conformational and topological quantities in a wide range of shear rates exhibited that the GENERIC MC is capable of predicting the general trends of structural response of entangled polymer systems to the applied flow. On the other hand, systematic quantitative discrepancies were observed between GENERIC MC and NEMD in the intermediate-to-strong flow regime. This is mainly attributed to the inherent mean-field nature of the GENERIC MC flow field which is uniformly and independently applied to each entanglement segments along the chains. Therefore, the GENERIC MC method would not be able to correctly predict physical properties and phenomena that involve flow-induced structural and dynamical correlations between different chain segments. Thus, the present MC methodology can be further improved by adequately incorporating the segmental correlations along the same chain and between different chains. This may be worth doing in future work.

In turn, the thermodynamic field tensor α obtained by the GENERIC MC simulations in conjunction with the NEMD can be used to evaluate fundamental thermodynamic information (such as the nonequilibrium configurational entropy and free energy functions) of flowing polymeric systems. The result of the thermodynamic field tensor can also be applied to analyze the capabilities of the existing viscoelastic models for entangled polymers and further develop more accurate general constitutive models. Furthermore, considering the basically same structural characteristics (i.e., chain orientation and stretch) for the backbone and long branches in response to the applied flow, it would be also interesting to apply the GENERIC MC method to the entangled branched polymers and analyze the distinctive rheological properties such as a steady-state tension thickening behavior for H-shaped polymer melts under elongational flows which is very difficult to examine by experiment or NEMD method. [1,5,52] Combining the advantages of the GENERIC MC and NEMD methods may allow us to carry out both basic and practical studies on complex rheological behaviors of large-scale entangled polymeric systems under various flowing conditions.

4.5. Reference

(1) R. B. Bird, R. C. Armstrong and O. Hassanger, *Dynamics of Polymeric Liquids, Fluid Mechanics*, John Wiley & Sons, New York, 2nd ed., 1987, vol. 1.

(2) F. A. Morrison, *Understanding Rheology*; Oxford University Press, New York, 2001.

(3) M. H. Wagner, H. Bastian, P. Hachmann, J. Meissner, S. Kurzbeck, H. Münstedt and F. Langouche, *Rheol. Acta.* 2000, **39**, 97-109.

(4) T. C. B. McLeish, *Adv. Phys.* 2002, **51**, 1379-1527.

(5) C. Baig and V. G. Mavrantzas, *J. Chem. Phys.* 2010, **132**, 014904.

(6) M. M. Denn, *Annu. Rev. Fluid Mech*. 2001, **33**, 265-287.

(7) R. Koopmans, J. den Doelder and J. Molenaar, *Polymer Melt Fracture*, CRC Press, Boca Raton, 2011.

(8) C. Baig, and B. J. Edwards, *Europhys. Lett.* 2010, **89**, 36003.

(9) K. Cui, Z. Ma, N. Tian, F. Su, D. Liu and L. Li, *Chem. Rev.* 2018, **118**, 1840-1886.

(10) R. S. Graham, *J. Rheol.* 2019, **63**, 203-214.

(11) A. N. Beris and B. J. Edwards, *Thermodynamics of Flowing Systems with Internal Microstructure,* Oxford University Press, New York, 1994.

(12) J. D. Moore, S. T. Cui, H. D. Cochran and P. T. Cummings, *J. Non-Newtonian Fluid Mech.* 2000, **93**, 83-99.

(13) J. M. Kim, D. J. Keffer, M. Kröger and B. J. Edwards, *J. Non-Newtonian Fluid Mech.* 2008, **152**, 168-183.

(14) C. Baig, V. G. Mavrantzas and M. Kröger, *Macromolecules* 2010, **43**, 6886-6902.\

(15) J. M. Kim, and C. Baig, *J. Chem. Phys.* 2016, **144**, 081101.

(16) J. Yoon, J. Kim and C. Baig, *J. Rheol.* 2016, **60**, 673-685.

(17) S. Jeong, S. Cho, J. M. Kim and C. Baig, *J. Rheol.* 2017, **61**, 253-264.

(18) S. Jeong, J. M. Kim and C. Baig, *Macromolecules* 2017, **50**, 3424-3429.; S. Jeong, J. M. Kim and C. Baig, *J. Chem. Phys.* 2017, **147**, 234901.

(19) M. H. Nafar Sefiddashti, B. J. Edwards and B. Khomami, *J. Rheol.* 2016, **60**, 1227-1244.

(20) M. P. Allen and D. J. Tildesley, *Computer Simulation of Liquids,* Clarendon Press, New York, 1987.

(21) D. Frenkel and B. Smit, *Understanding Molecular Simulation,* Academic Press, London, 2nd ed., 2002.

(22) M. Grmela and H. C. Öttinger, *Phys. Rev. E* 1997, **56**, 6620-6632.

(23) H. C. Öttinger and M. Grmela, *Phys. Rev. E* 1997, **56**, 6633-6655.

(24) H. C. Öttinger, *Beyond Equilibrium Thermodynamics,* John Wiley & Sons, New Jersey, 2005.

(25) V. G. Mavrantzas and D. N. Theodorou, *Macromolecules* 1998, **31**, 6310-6332.

(26) V. G. Mavrantzas and H. C. Öttinger, *Macromolecules* 2002, **35**, 960-975.

(27) V. G. Mavrantzas and D. N. Theodorou, *Macromol. Theory Simul.* 2000, **9**, 500-515.

(28) C. Baig and V. G. Mavrantzas, *Phys. Rev. Lett.* 2007, **99**, 257801.

(29) C. Baig and V. G. Mavrantzas, *Phys. Rev. B* 2009, **79**, 144302.

(30) C. Baig and B. J. Edwards, *J. Non-Newtonian Fluid Mech.* 2010, **165**, 992-1004.

(31) R. B. Bird, C. F. Curtiss, R. C. Armstrong and O. Hassager, *Dynamics of Polymeric Liquids*, *Kinetic Theory,* John Wiley & Sons, New York, 2nd ed., 1987, vol. 2.

(32) G. T. Dee, T. Ougizawa and D. J. Walsh, *Polymer* 1992, **33**, 3462-3469.

(33) C. Baig, V. G. Mavrantzas and H. C. Öttinger, *Macromolecules* 2011, **44**, 640-646.

(34) L. J. Fetters, D. J. Lohse, D. Richter, T. A. Witten and A. Zirkel, *Macromolecules* 1994, **27**, 4639-4647.

(35) P. G. de Gennes, *J. Chem. Phys.* 1971, **55**, 572-579.

(36) M. Doi and S. F. Edwards, *The Theory of Polymer Dynamics,* Clarendon Press, New York, 1986.

(37) V. G. Mavrantzas, T. D. Boone, E. Zervopoulou and D. N. Theodorou, *Macromolecules* 1999, **32**, 5072-5096.

(38) C. Baig, O. Alexiadis and V. G. Mavrantzas, *Macromolecules* 2010, **43**, 986-1002.

(39) C. Baig, B. J. Edwards, D. J. Keffer and H. D. Cochran, *J. Chem. Phys.* 2006, **124**, 084902.

(40) S. Nosé, *Mol. Phys.* 1984, **52**, 255-268.

(41) W. G. Hoover, *Phys. Rev. A* 1985, **31**, 1695-1697.

(42) A. W. Lees and S. F. Edwards, *J. Phys. C: Solid State Phys.* 1972, **5**, 1921-1929.

(43) M. Tuckerman, B. J. Berne and G. J. Martyna, *J. Chem. Phys.* 1992, **97**, 1990-2001.

(44) J. I. Siepmann, S. Karaborni and B. Smit, *Nature* 1993, **365**, 330-332.

(45) J. M. Kim, B. J. Edwards, D. J. Keffer and B. Khomami, *Phys. Lett. A* 2009, **373**, 769-772.

(46) V. Venkataramani, R. Sureshkumar and B. Khomami, *J. Rheol.* 2008, **52**, 1143-1177.

(47) J. M. Kim, B. J. Edwards, D. J. Keffer and B. Khomami, *J. Rheol.* 2010, **54**, 283-310.

(48) S. H. Jeong, J. M. Kim and C. Baig, *J. Rheol.* 2018, **62**, 1115-1124.

(49) S. Cho, S. Jeong, J. M. Kim and C. Baig, *Sci. Rep.* 2017, **7**, 9004.

(50) M. Kröger, *Comput. Phys. Commun.* 2005, **168**, 209-232.

(51) S. H. Jeong, J. M. Kim, J. Yoon, C. Tzoumanekas, M. Kröger and C. Baig, *Soft Matter* 2016, **12**, 3770-3786.

(52) H. Münstedt and H. M. Laun, *Rheol. Acta.* 1981, **20**, 211-221

Acknowledgement

I would like to express my deepest gratitude to my advisor, Prof. Chunggi Baig, for his enthusiasm, patience, and guidance throughout my Ph.D. study at UNIST. His encouraging me to develop as an independent researcher has been invaluable.

I also wish to appreciate to Prof. Jun Mo Kim for the instructive discussions and helpful communication. In addition, I would like to thank to Prof. So Youn Kim, Prof. Jaeup Kim, Prof. Jiseok Lee, and Prof. Hankwon Lim for the willingness to serve on my Ph.D. committee and their hard questions and insightful comments to enhance my doctoral dissertation.

My thanks goes to group members in Theoretical and Computational study of Polymers & Nanomaterials Laboratory; Jeongha Yoon, Miran Ha, Jinseong Kim, Seung Heum Jeong, Soowon Cho, Ukjung Kang, and Tae Yong Ha.

Also, I owe a very special debt of gratitude to all my family; Seung Chan Bang, Eun Yeong Noh, Ro Geon Bang, and my lovely little sister Eun Gyeong Noh for giving me unfailing love and support throughout my life.

Last, I would like to dedicate my Ph.D. dissertation to my love Sukhwan Kang who always trusted that I could make it and motivated me to achieve my goals.